Electronic Supplementary Material (ESI) for Molecular Systems Design & Engineering.

Supporting Information

Bis ferrocenyl-hydrazide metal complexes: Studying electronic functional groups as newly potent homogeneous photocatalysts for C(sp^3)-H and C(sp^2)-H bonds oxidation utilizing visible light condition

Mohammad Bashiri[1], Mona Hosseini-Sarvari[1*], and Sara Fakhraee[2]

[1]Nanophotocatalysis Lab., Department of Chemistry, Shiraz University, Shiraz 7194684795, I.R. Iran.

[2] Department of Chemistry, Payame Noor University, 19395-3697, Tehran, Iran.

Email: ✉ hossaini@shirazu.ac.ir

List of Contents

Hand-made photoreactor system.....S3

The emission spectrum of LED lamps S4

Experimental section.....S4

Methods…….....S4

The method of HPLC with UV detector.....S5

A general method to study Redox behavior S5

A general method to study photocurrent….....S5

Analytical data of the synthesized products.....S6

Ferrocenyl-hydrazide Schiff base (FcHz-X) 3a-c.....S6

Bis ferrocenyl-hydrazide attached nickel ([$(FcHz)_2$Ni]) 4a….....S6

Bis ferrocenyl-hydrazide attached copper ([$(FcHz)_2$Cu]) 5b.....S6

Indoline-2,3-dione 3d.....S6

Cyclic Voltammetry of ([$(FcHz)_2$Ni]) and ([$(FcHz)_2$Cu]) S7

XRF graphs…….....S8

SEM micrographs investigation…….....S11

EDX investigation.…….....S12

Extinction coefficient of the synthesized complexes.....S13

NMR and HPLC graphs…….....S14

Theorical IR study……..…….....S30

References S32

Hand-made photoreactor system

To utilization of visible light irradiation and inexpensive high-energy LEDs, we decided to design a suitable batch optical system to investigate the photocatalytic properties of our complexes. The Beer−Lambert law indicates that the photon flux is directly proportional to the distance, and the photon flux decreases with increasing depth in a reaction medium[1]. Therefore, for photocatalytic reactions, it is so reasonable that the reaction medium is close to radiation. We attempted to illustrate an integrated photoreactor that would deliver cooling, shaking, usable simplicity and most importantly, highly matchable results. In this system, several positions are installed for the reaction medium, which is closest to the radiation. A noteworthy point in this system is the radiation of light from below to the reaction medium. A distance of 1cm was established between the test tube and LED array to absorb photons. For united mixing, a commercial stirrer with 2300 rpm (IKA and Heidolph) with a magnet was used. Four LED powers (3W) are connected in series and a total of 12W radiates to the medium reaction. LED powers (12W) with different wavelengths in the visible region were prepared and placed on the aluminum heatsink. So, the reaction medium is then irradiated with light from below. One feature added to the design is the ability to control the intensity of radiant light. A test tube holder set was illustrated to incorporate various test tube sizes such as 12, 16, 20 mm tubes allowing routine reaction scales from millimolar to gram scale. These tube positions certify stable placement while keeping the optimum test tube-to-LED distance. In order to cool the reaction medium and LEDs, a thermobox was used where water flow is possible with a pump. Views of the in-hand photoreactor are displayed in Figure S1.

Figure S1. Novel LEDs setup to display high photon offer to the reaction medium

The emission spectrum of LED lamps:

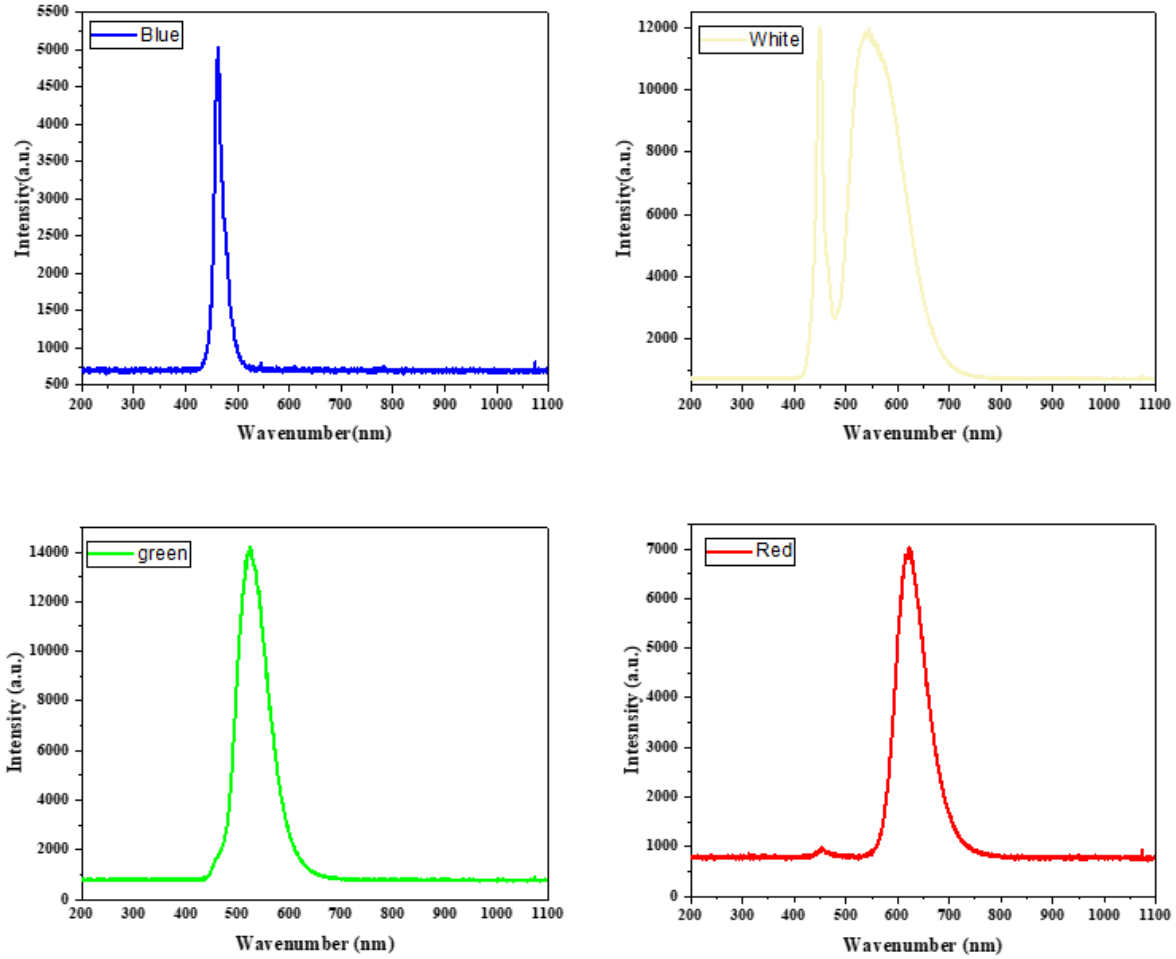

Figure S2. Emission spectrum of LED lamps used in photocatalysis reaction

1. Experimental section:

All beginning compounds have been obtained from basic chemical factories such as Acros Organic, Fluka, Merck, and Sigma-Aldrich which were used without further purification. Materials and solvents were dried before use. Different methods have been used to detect the structure of synthesized compounds such as FT-IR analysis, ^{1}H and ^{13}C NMR spectral information, X-ray diffraction analysis (XRD), X-ray fluorescence (XRF), elemental analysis, cyclic voltammetry, scanning electron microscope (SEM), energy dispersive X-ray analysis (EDX), thermogravimetric analysis (TGA), UV-visible. Fourier-transform infrared spectroscopies were provided on a TENSOR II in the frequency range between 400 to 4000 (ν in cm^{-1}). ^{1}H NMRs were recorded on a Bruker Avance III 400 MHz and using $CDCl_3$ and DMSO-d_6 with tetramethylsilane (TMS) as an internal standard, ^{13}C NMRs were recorded on a Bruker Avance III 100 MHz and using $CDCl_3$ and DMSO-d_6 with tetramethylsilane (TMS) as an internal standard. Chemical shifts are reported in parts per million (δ) deshield from TMS and coupling constant (^{n}J) are shown in (Hz) Hertz. Hydrogen signal splitting templates are indicated for the multiplicities: *s*: singlet, *d*: doublet, *t*: triplet, *q*: quartet, *dd*: doublet of doublet, *m*: multiplet, and *br*: broad, signal for proton spectra. Elementa analyses were recorded on a Thermo Finnigan Flash EA-1112. The XRFs were recorded on Unisantis XMF 104. The SEM and EDX analyses were obtained by TESCAN-Vega 3. Fluorescence spectroscopy were run by Varian Cary Eclipse. UV-visible spectroscopy was run by Biochrom WPA Biowave II. The TGA was used by investigate the thermal stability of samples by SDT Q600 V20.9 build 20 analyzer. Cyclic voltammetry was investigated with autolab 84490. For analyzing products, High Performance Liquid Chromatography (HPLC) was used (AZURA, Germany). To determine the X-ray diffraction pattern of the nano organo-metal compounds, XRD technique was followed by applying Bruker D-8ADVANCE with a CuKa irradiation source (1.5406 Å). The 2θ angle was scanned at a rate of 1.5 ^{o}/ min within the 2θ=5-90^{o}.

1.1. Methods:

1.1.1. The method of HPLC with UV detector:

Chromatographic conditions: Chromatographic separations were performed at ambient temperature and was run utilizing column C18 by an injection volume of 5-20 µL. The mobile phase in acetonitrile–water (35:65, v/v) at a flow rate of 1 mL/min was applied to C18 column. The wavelength of the UV detector was fixed at 254 nm.

1.1.2. A general method to study Redox behavior:

The electronic properties of Fc, FcHz-X, [(FcHz-X)$_2$Ni] and [(FcHz-X)$_2$Cu] were examined by applying cyclic voltammetry (CV). The measurements were achieved at 25 ^{o}C with ~10^{-3} M dimethylformamide solutions of the ferrocene-based compounds containing 0.1 M tetrabutylammonium bromide as supporting electrolyte. In this study a platinum electrode was used as a working electrode and a platinum wire was employed as the auxiliary electrode and a wire of Ag/AgCl as a reference electrode.

1.1.3. A general method to study photocurrent:

The photocurrent examination was recorded on an electrochemical instrument in a standard three-electrode with a Pt wire as the working electrode, FTO as the counter electrode and Ag/AgCl (sutured KCl) as a reference electrode. A Xe arc lamp *via* a UV-separator filter (λ> 400 nm) was used as a light source with an intensity of 0.6 V applied potential. Na_2SO_4 (0.5 M) aqueous solution was used as the electrolyte.

2. Analytical data of the synthesized products:

2.1. Ferrocenyl-hydrazide Schiff base (FcHz) 3a:

Brown powder, isolated yield: 80.4%, FT-IR: $\bar{\nu}$= 3300-3500 (NH amide), 1643 (C=O amide), 1604 (C=N imine), ^{1}H NMR (400 MHz, DMSO-d_6) δ 11.43 (s, 1H, NH), 8.26 (s, 1H, N=CH), 7.87 – 7.85 (m, 2H, aromatic H), 7.47 – 7.41 (m, 3H, aromatic H), 4.62 – 4.54 (m, 2H, Fc H), 4.34 – 4.30 (m, 2H, Fc H), 4.14 – 4.12 (m, 5H, Fc H).

2.2. Ferrocenyl-hydrazide Schiff base (FcHz-OH) 3b:

Brown powder, isolated yield: 85.3%, FT-IR: $\bar{\nu}$= 3300-3500 (NH amide), 1647 (C=O amide), 1605 (C=N imine), ^{1}H NMR (300 MHz, DMSO-d_6) δ 11.43 (s, 1H, NH), 10.24 (s, 1H, OH), 8.24 (s, 1H, N=CH), 7.79 (d, J = 8.0 Hz, 2H, aromatic H), 6.85 (d, J = 8.0 Hz, 2H, aromatic H), 4.67 – 4.60 (m, 2H, Fc H), 4.46 – 4.39 (m, 2H, Fc H), 4.24 – 4.16 (m, 5H, Fc H).

2.3. Ferrocenyl-hydrazide Schiff base (FcHz-NO_2) 3c:

Red powder, isolated yield: 79.5%, FT-IR: $\bar{\nu}$= 3300-3500 (NH amide), 1667 (C=O amide), 1597 (C=N imine), ^{1}H NMR (400 MHz, Chloroform-d and DMSO-d_6) δ 11.30 (s, 1H), 8.20 (s, 1H), 8.17 – 8.14 (m, 2H), 8.05 – 8.00 (m, 2H), 4.60 – 4.54 (m, 2H), 4.30 – 4.26 (m, 2H), 4.09 – 4.05 (m, 5H).

2.4. Bis ferrocenyl-hydrazide attached nickel ([(FcHz)$_2$Ni]) 4a:

Red powder, isolated yield: 68.3%, FT-IR (KBr): $\bar{\nu}$= 1604 (C=N imine), 1581 (C=O amide), 1411 (C=C ferrocene) cm^{-1}, ^{1}H NMR (400 MHz, DMSO-d_6) δ 9.71 (s, 2H), 7.96 – 7.91 (m, 1H), 7.88 (d, J = 7.0 Hz, 1H), 7.76 – 7.58 (m, 2H), 7.53 – 7.44 (m, 2H), 7.41 – 7.32 (m, 3H), 7.24 – 7.16 (m, 1H), 7.09 – 7.01 (m, 1H), 6.65 (s, 1H), 6.58 – 6.56 (m, 1H), 6.48 (d, J = 4.9 Hz, 1H), 6.08 – 5.88 (m, 1H), 5.78 – 5.66 (m, 1H), 5.55 – 5.39 (m, 2H), 5.28 – 5.22 (m, 1H), 4.68 – 4.59 (m, 2H), 4.42 – 4.10 (m, 8H).

2.5. Bis ferrocenyl-hydrazide attached copper ([(FcHz)$_2$Cu]) 5b:

Red powder, isolated yield: 69.5%, FT-IR (KBr): $\bar{\nu}$= 1612 (C=N imine), 1566 (C=O amide), 1411 (C=C ferrocene) cm^{-1}, ^{1}H NMR (400 MHz, DMSO-d_6) δ 9.79 (s, 2H), 7.99 – 7.82 (m, 2H), 7.74 – 7.63 (m, 2H), 7.54 – 7.45 (m, 2H), 7.41 – 7.31 (m, 2H), 7.24 – 7.13 (m, 1H), 7.12 – 6.95 (m, 1H), 6.64 – 6.35 (m, 4H), 5.64 – 5.28 (m, 4H), 4.78 – 4.59 (m, 2H), 4.42 – 4.22 (m, 8H).

2.6. *P*-nitrobenzaldehyde (6b):

^{1}H NMR (300 MHz, Chloroform-d) δ 10.17 (s, 1H), 8.40 (d, J = 8.5 Hz, 2H), 8.09 (d, J = 8.5 Hz, 2H); ^{13}C NMR (75 MHz, Chloroform-d) δ 190.41, 151.08, 140.03, 130.52, 124.31.

2.7. *P*-nitrobenzoic acid (6c):

^{1}H NMR (300 MHz, DMSO-d_6) δ 13.71 (s, 1H), 8.30 (d, J = 8.9 Hz, 2H), 8.15 (d, J = 8.9 Hz, 2H); ^{13}C NMR (75 MHz, DMSO-d_6) δ 166.25, 150.42, 136.79, 131.13, 124.15.

2.8. Indoline-2,3-dione 8b:

Orange powder, isolated yield: 45.1%, ^{1}H NMR (400 MHz, Chloroform-d) δ 10.55 (s, 1H, NH), 7.37 (t, J = 7.8 Hz, 2H, aromatic H), 6.90 (t, J = 7.5 Hz, 1H, aromatic H), 6.79 (d, J = 7.8 Hz, 1H, aromatic H), ^{13}C NMR (101

MHz, Chloroform-*d*) δ 184.55 (^{2}C=O of isatin), 159.62 (^{1}C=O of isatin), 150.85, 138.43, 125.11, 123.10, 117.70, 112.59.

Cyclic Voltammetry of ([(FcHz)$_2$Ni]) and ([(FcHz)$_2$Cu]):

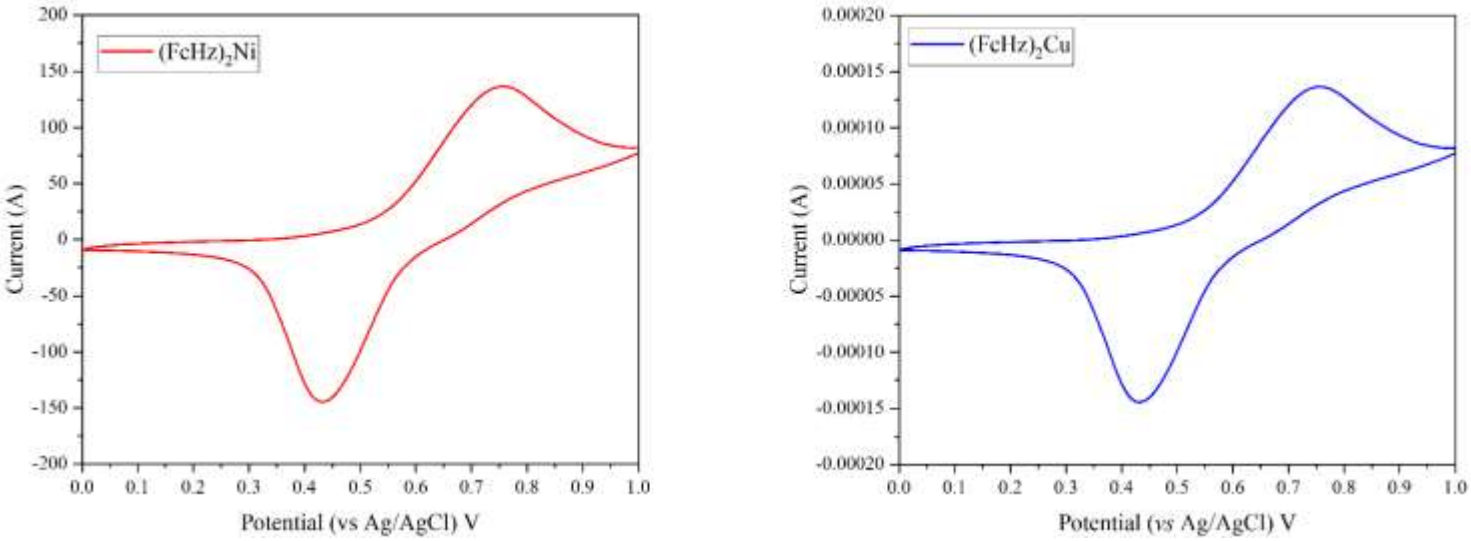

Figure S3. Cyclic voltammograms of FcHz)$_2$Ni and FcHz)$_2$Cu

XRF analysis spectrum:

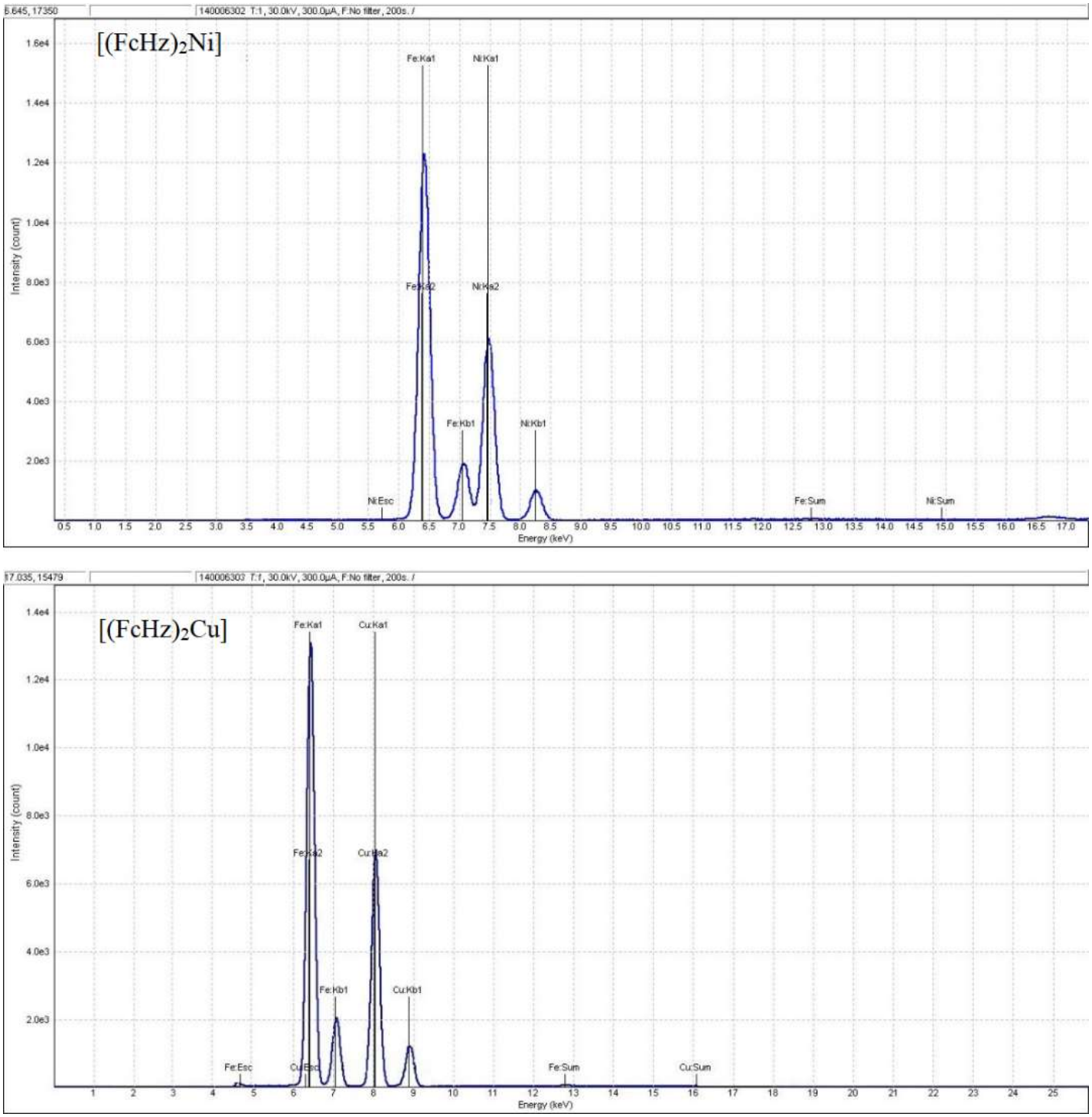

Figure S4. XRF analysis for $[(FcHz)_2Ni]$ and $[(FcHz)_2Cu]$

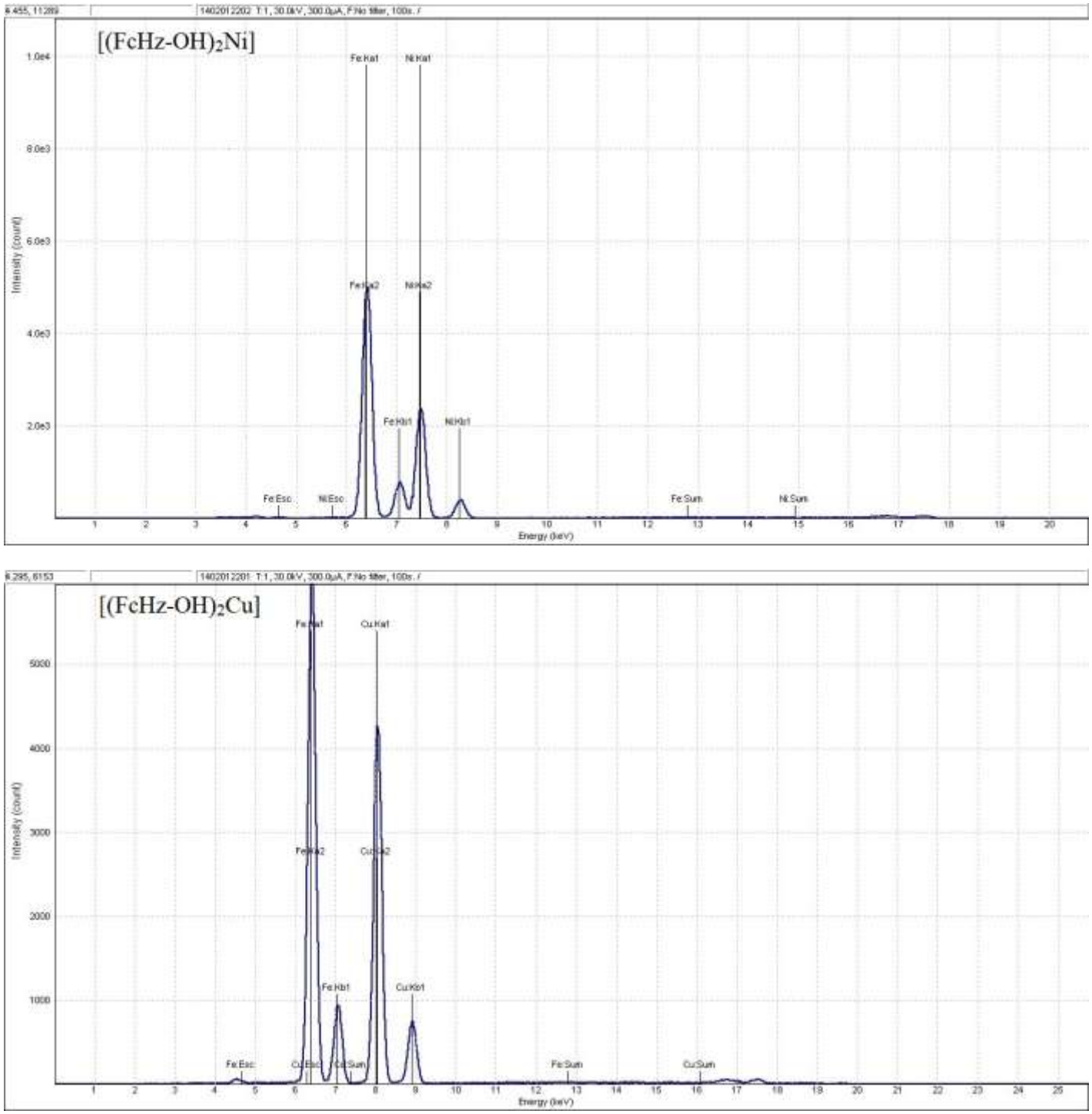

Figure S5. XRF analysis for [(FcHz-OH)$_2$Ni] and [(FcHz-OH)$_2$Cu]

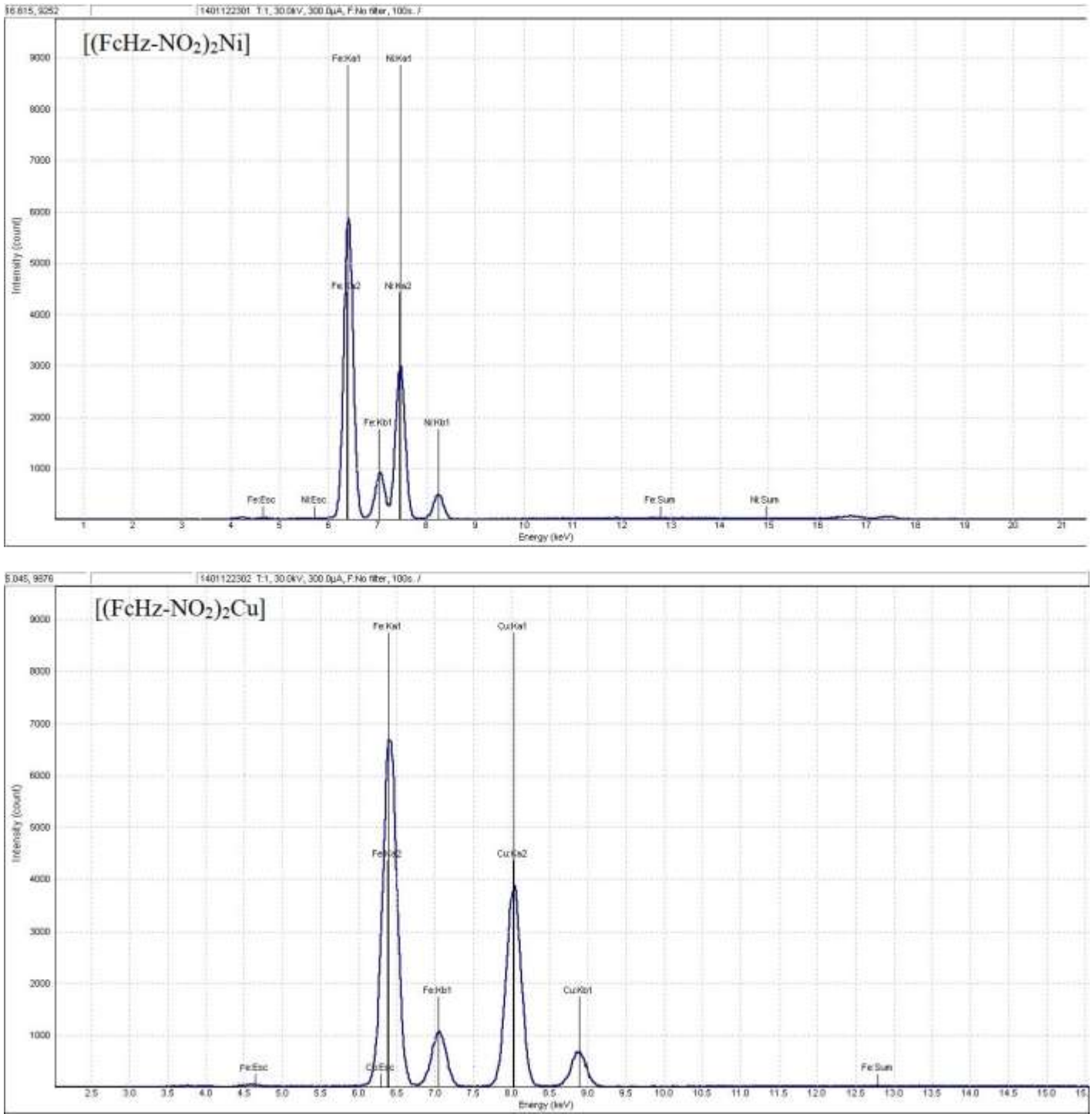

Figure S6. XRF analysis for [(FcHz-NO_2)$_2$Ni] and [(FcHz-NO_2)$_2$Cu]

SEM micrographs investigation:

A scanning electron microscope (SEM) was used to see the morphological differences between the $[(FcHz)_2Ni]$ and $[(FcHz)_2Cu]$ complexes (Figures S6a-d). The SEM micrographs of complexes displayed the distribution of particles in Ni and Cu complexes as clusters of irregularly shaped arranged. High magnification of SEM pictures indicated that these metal complex particles have irregular shapes. From the comparison of the SEM micrographs of $[(FcHz)_2Ni]$ and $[(FcHz)_2Cu]$ can be concluded that the Ni complex has crystals in a similar arrangement to the particles of the Cu complex.

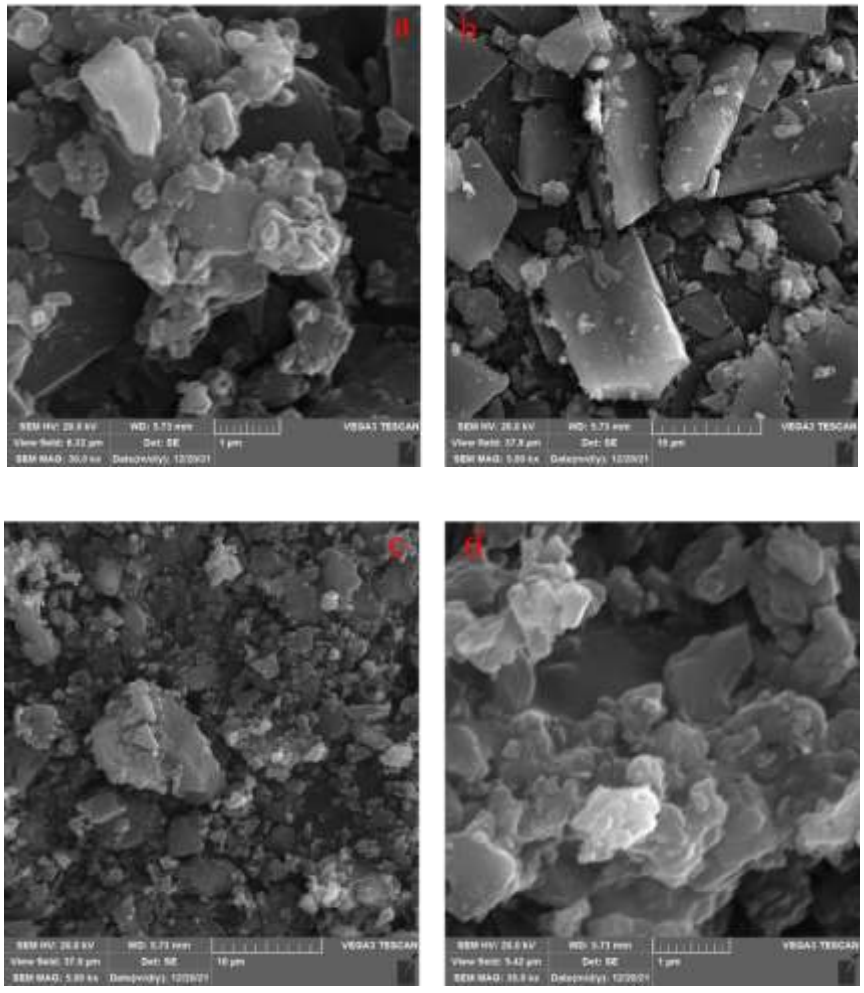

Figure S7. Scanning electron micrograph (SEM) of (a, b): $[(FcHz)_2Ni]$ **(**c, d): $[(FcHz)_2Cu]$ with various magnifications

EDX investigation:

The EDX analysis was introduced for studying the successful coordination of Ni and Cu to the FcHz ligand. The EDX's graph is illustrated in Figure S7. From EDX spectra we found that Ni, as well as Cu, attached on FcHz. According to the analyses, the peaks of C, N, and O are attributed to the benzohydrazide and cyclopentadienyl rings. As well as, the relative peaks of Ni and Cu showed that these metals coordinated with ferrocenyl ligands. The peaks of Fe confirmed the presence of iron atoms in entire complexes $[(FcHz)_2Ni]$ and $[(FcHz)_2Cu]$. Quantitative analyses of the EDX results are shown in Table S1. The EDX results demonstrate that the desired complex has been synthesized successfully, with the expected ratios.

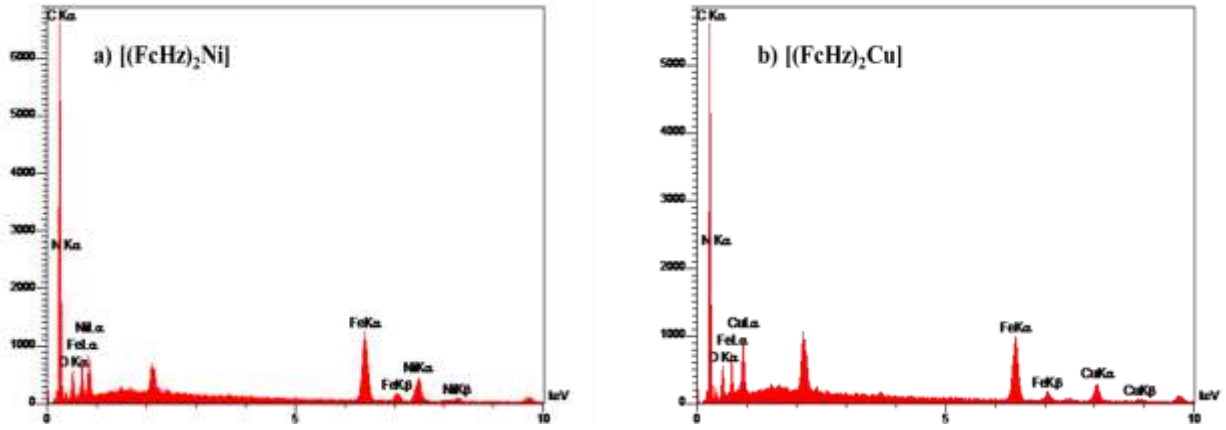

Figure S8. EDX of a) $[(FcHz)_2Ni]$ and b) $[(FcHz)_2Cu]$

Table S1. Percentage weight of elements and atoms obtained from EDX analysis for $[(FcHz)_2Ni]$ and $[(FcHz)_2Cu]$ complexes

Compound	Elements	Element, % weight	Atom, %
	C	60.36	71.07
	O	11.46	10.13
$[(FcHz)_2Ni]$	N	15.49	15.64
	Fe	8.17	2.07
	Ni	4.53	1.09
	C	58.29	68.64
	O	12.94	11.44
$[(FcHz)_2Cu]$	N	16.87	17.04
	Fe	7.60	1.92
	Cu	4.30	0.96

Extinction coefficient of the synthesized complexes:

In order to determine the extinction coefficient, the synthesized samples were prepared in a solvent of H_2O: DMF (1:1) at a certain concentration. The absorption spectrum of these samples was then taken at various concentrations, and an absorption graph was plotted based on the concentration. The slope of the graph was used to report the extinction coefficient.

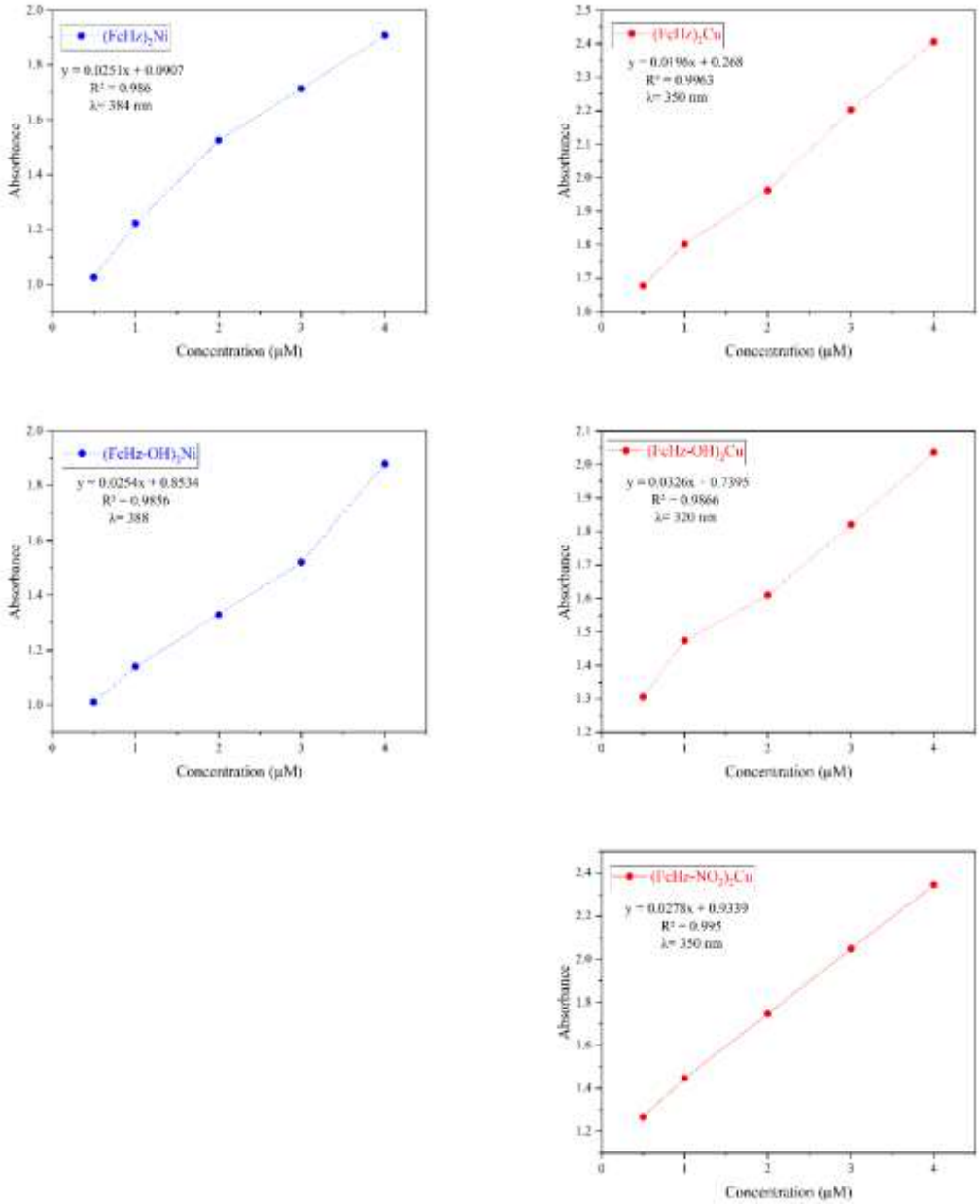

Figure S9. Extinction coefficient of the synthesized complexes

2.9. ^{1}H NMR spectroscopies of (FcHz) 3a:

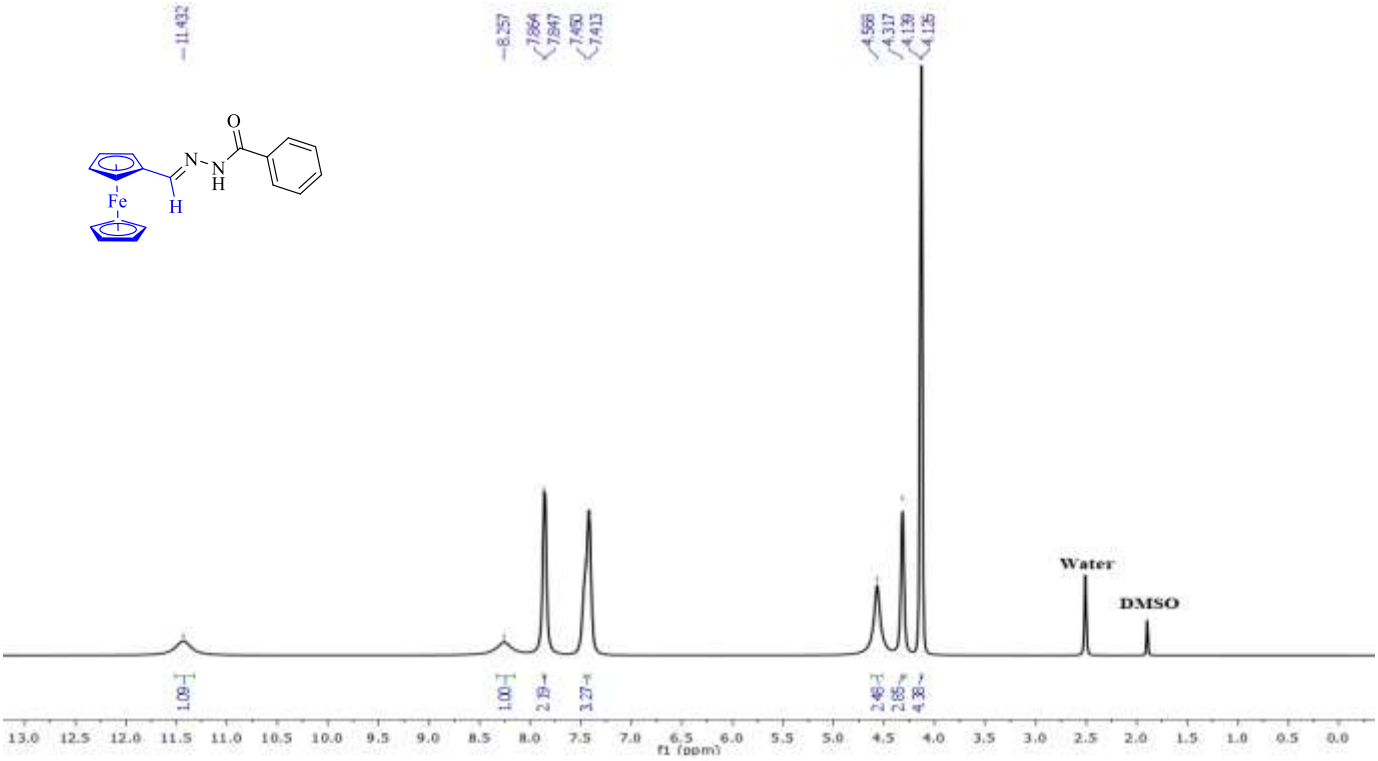

Figure S10. ^{1}H NMR (400 MHz) of ferrocenyl-hydrazide Schiff base (FcHz) **3a** in DMSO-*d6*

2.10. ^{1}H NMR spectroscopies of (FcHz-OH) 3b:

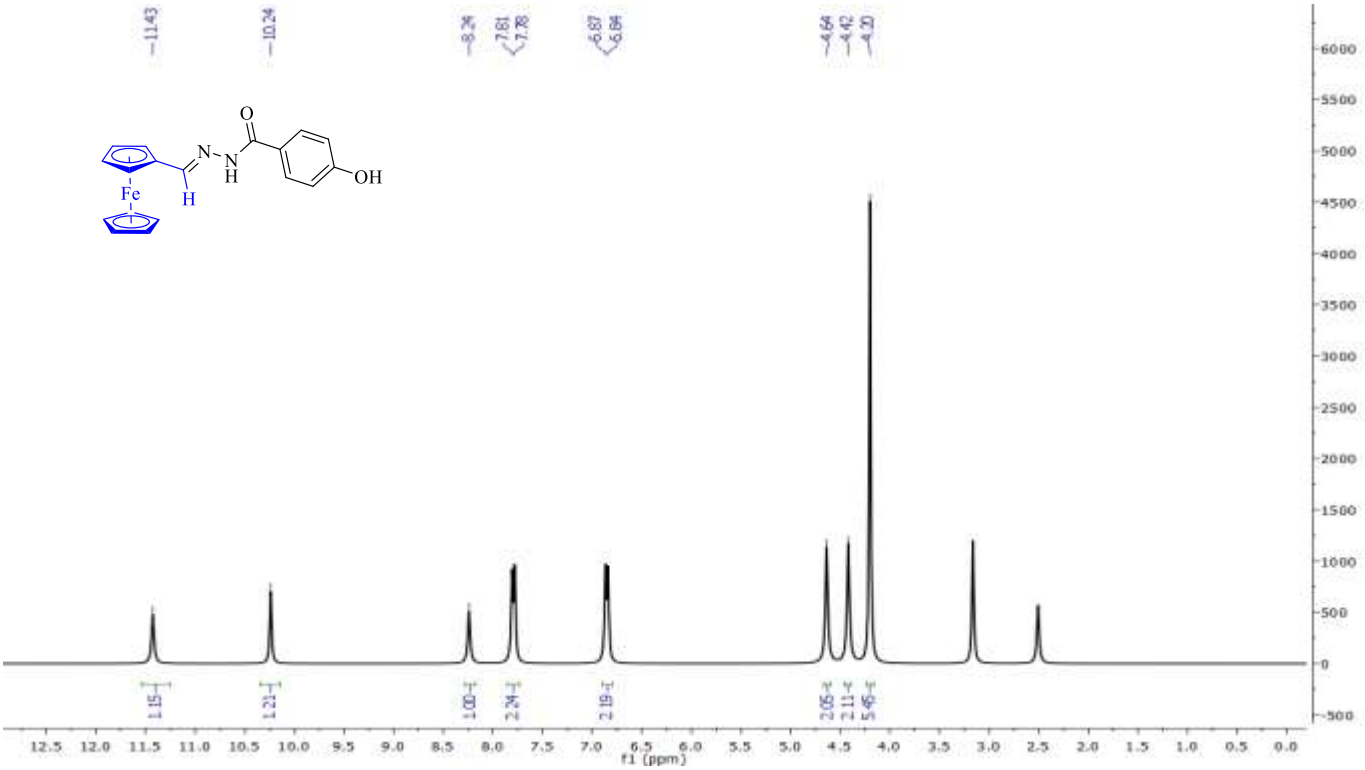

Figure S11. ^{1}H NMR (400 MHz) of ferrocenyl-hydrazide Schiff base (FcHz-OH) **3b** in DMSO-*d6*

2.11. ^{1}H NMR spectroscopies of (FcHz-NO_2) 3c:

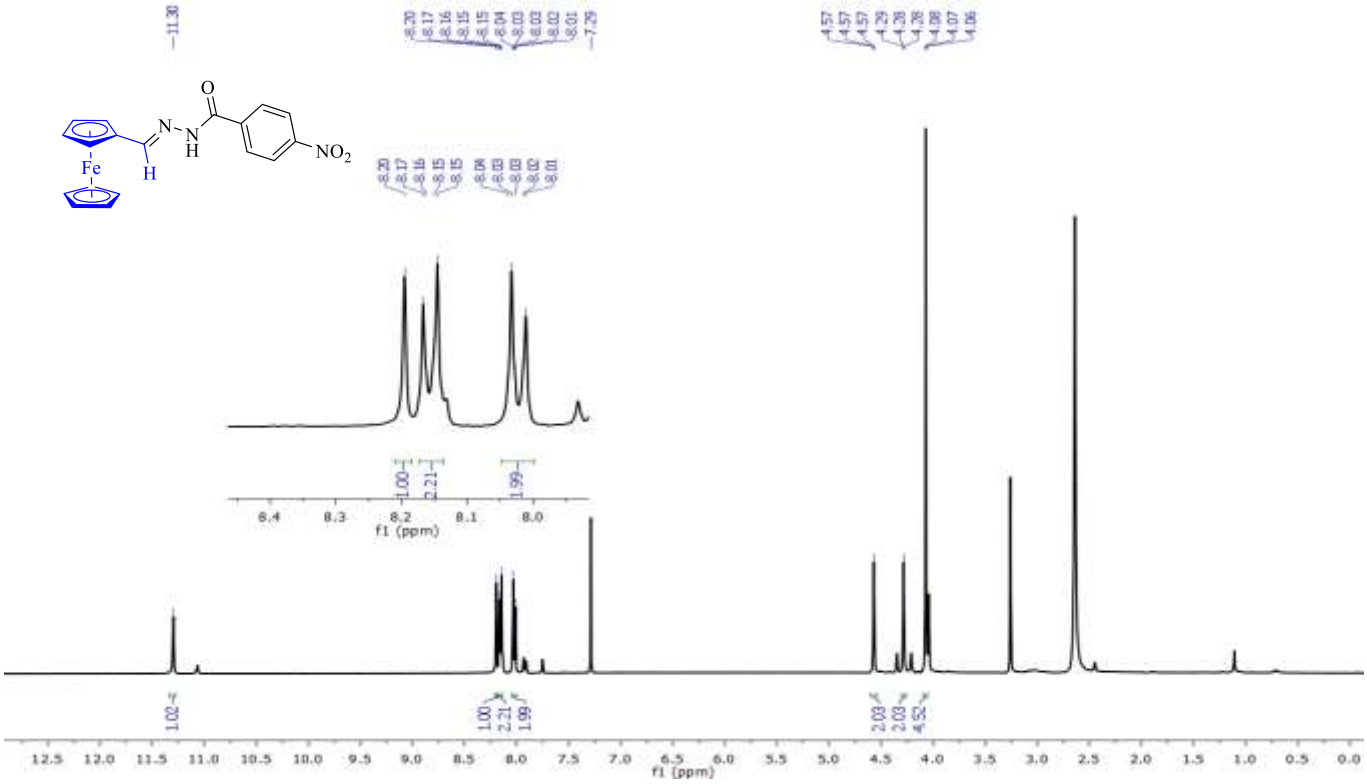

Figure S12. ^{1}H NMR (400 MHz) of ferrocenyl-hydrazide Schiff base (FcHz-NO_2) **3c** in $CDCl_3$ & DMSO-*d6*

2.12. ^{1}H NMR spectroscopies of Bis ferrocenyl-hydrazide attached nickel ([(FcHz)$_2$Ni]) 4a:

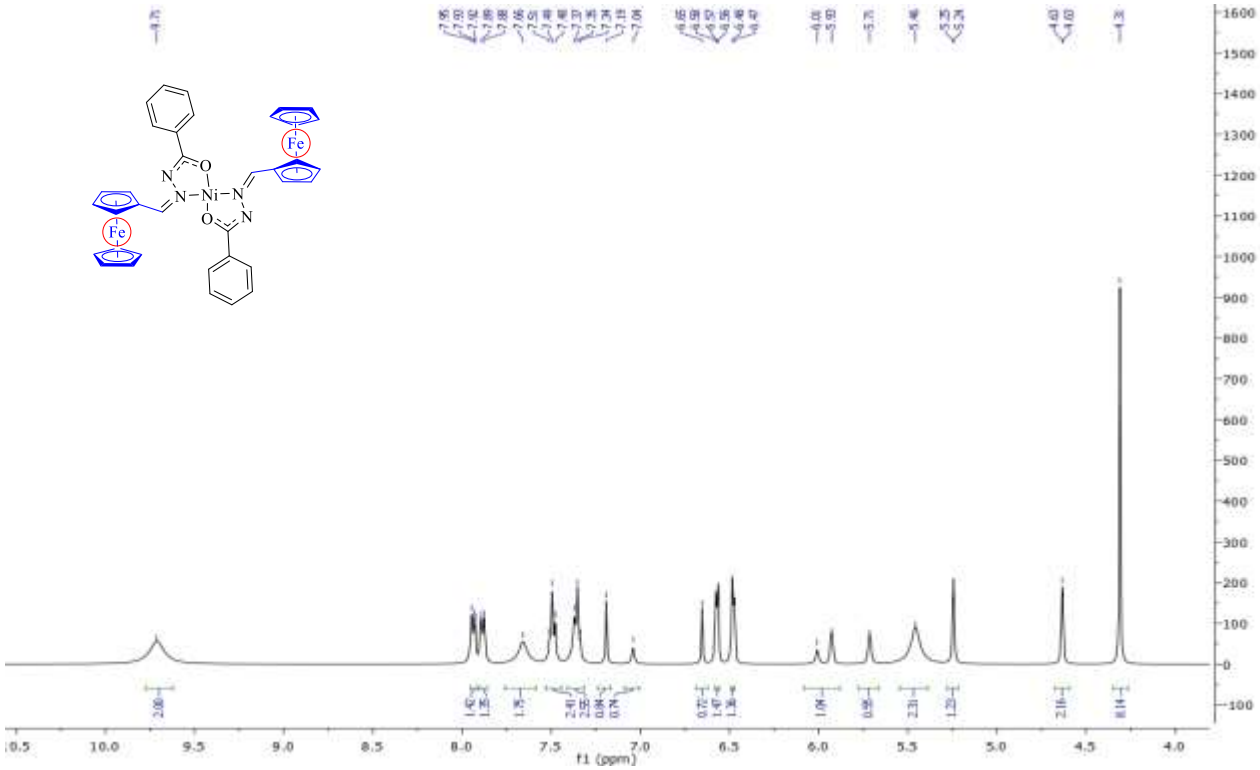

Figure S13. ^{1}H NMR (400 MHz) of Bis ferrocenyl-hydrazide attached nickel ([(FcHz)$_2$Ni]) **4a** in DMSO-*d6*

2.13. ^{1}H NMR spectroscopies of Bis ferrocenyl-hydrazide attached copper ([(FcHz)$_2$Cu]) 4b:

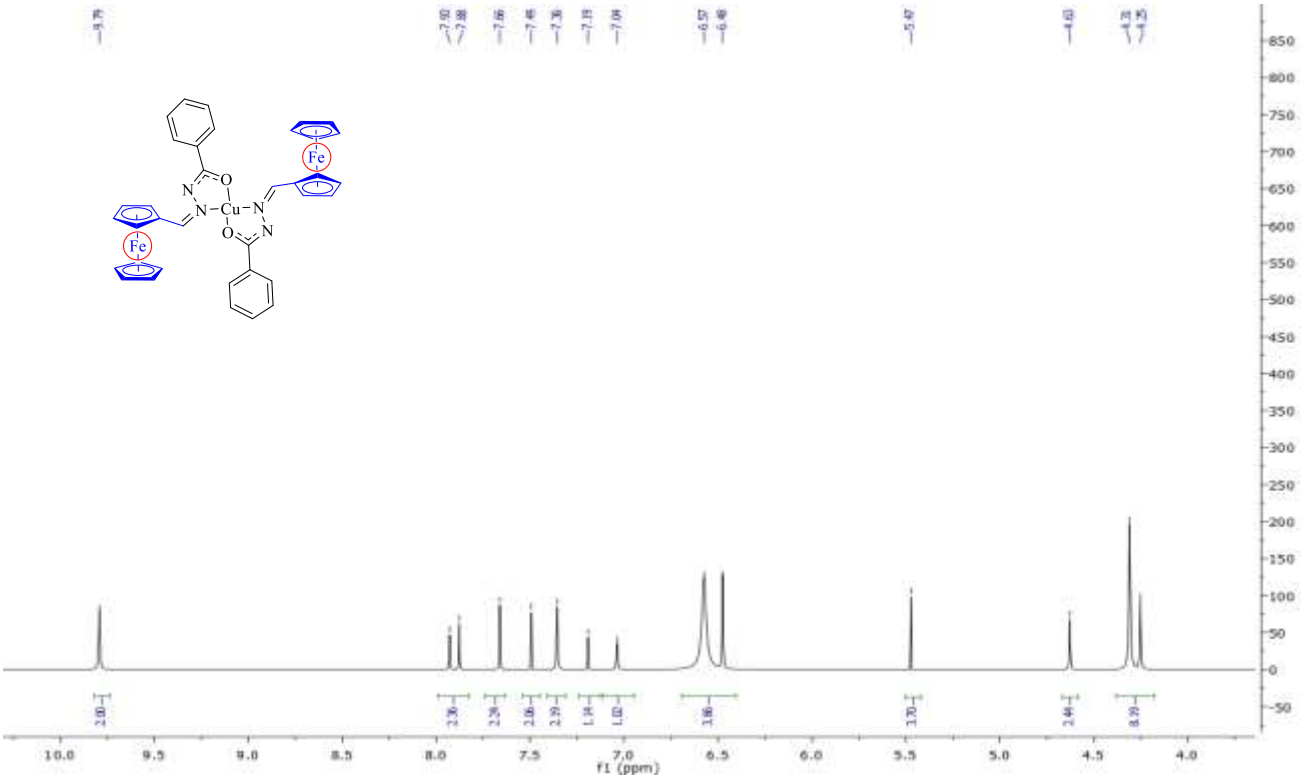

Figure S14. ^{1}H NMR (400 MHz) of Bis ferrocenyl-hydrazide attached nickel ([(FcHz)$_2$Cu]) **4b** in DMSO-*d6*

2.14. ^{1}H and ^{13}C NMR spectroscopies of *p*-nitrobenzaldehyde (6b):

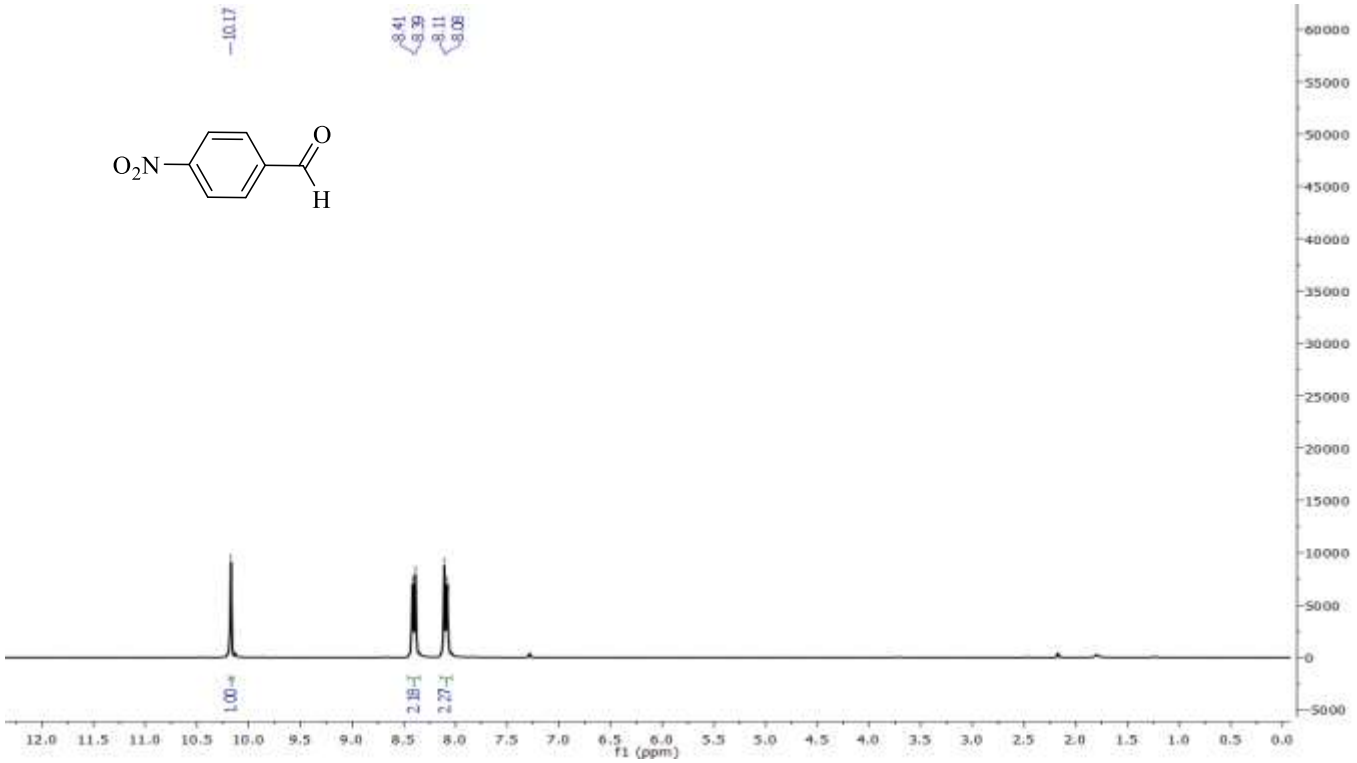

Figure S15. ^{1}H NMR (300 MHz) of *p*-nitrobenzaldehyde **6b** in DMSO-*d6*

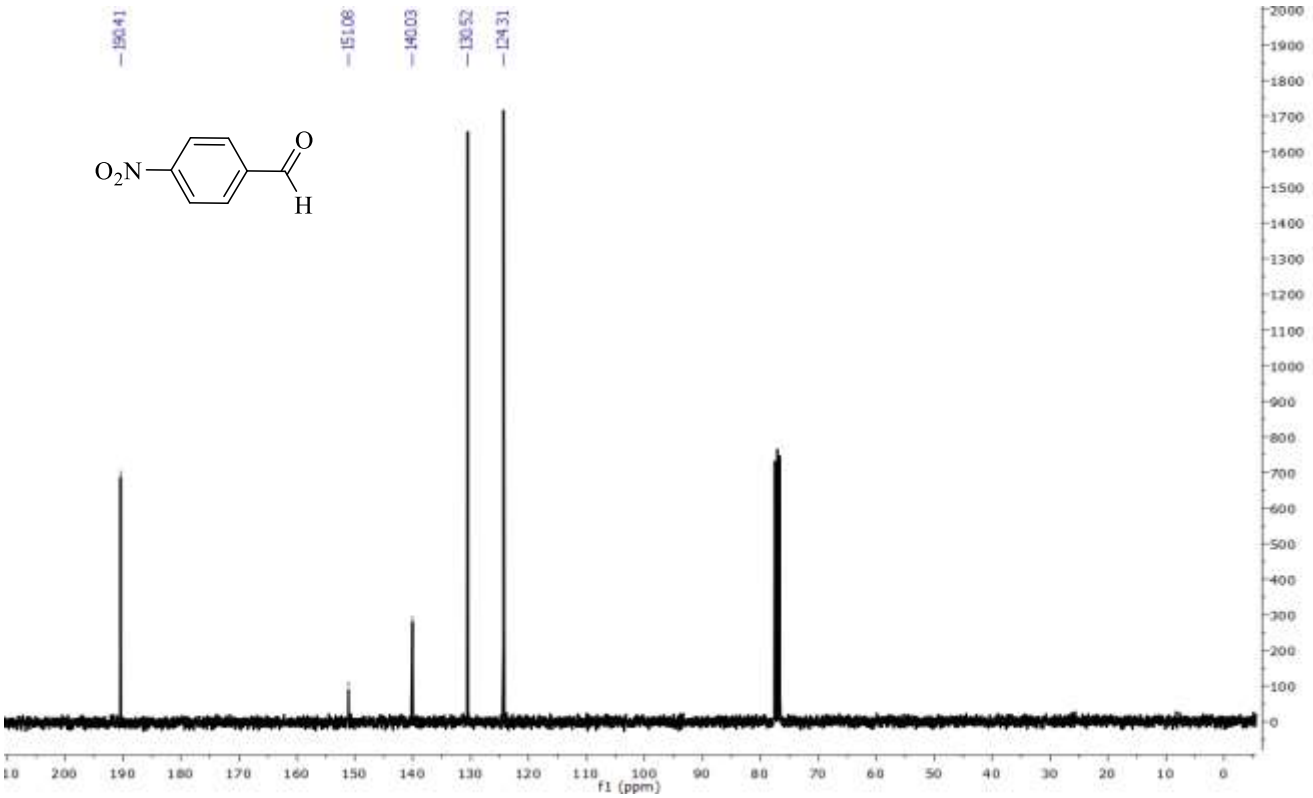

Figure S16. ^{13}C NMR (300 MHz) of *p*-nitrobenzaldehyde **6b** in DMSO-*d6*

2.15. ^{1}H and ^{13}C NMR spectroscopies of *p*-nitrobenzoic acid (6c):

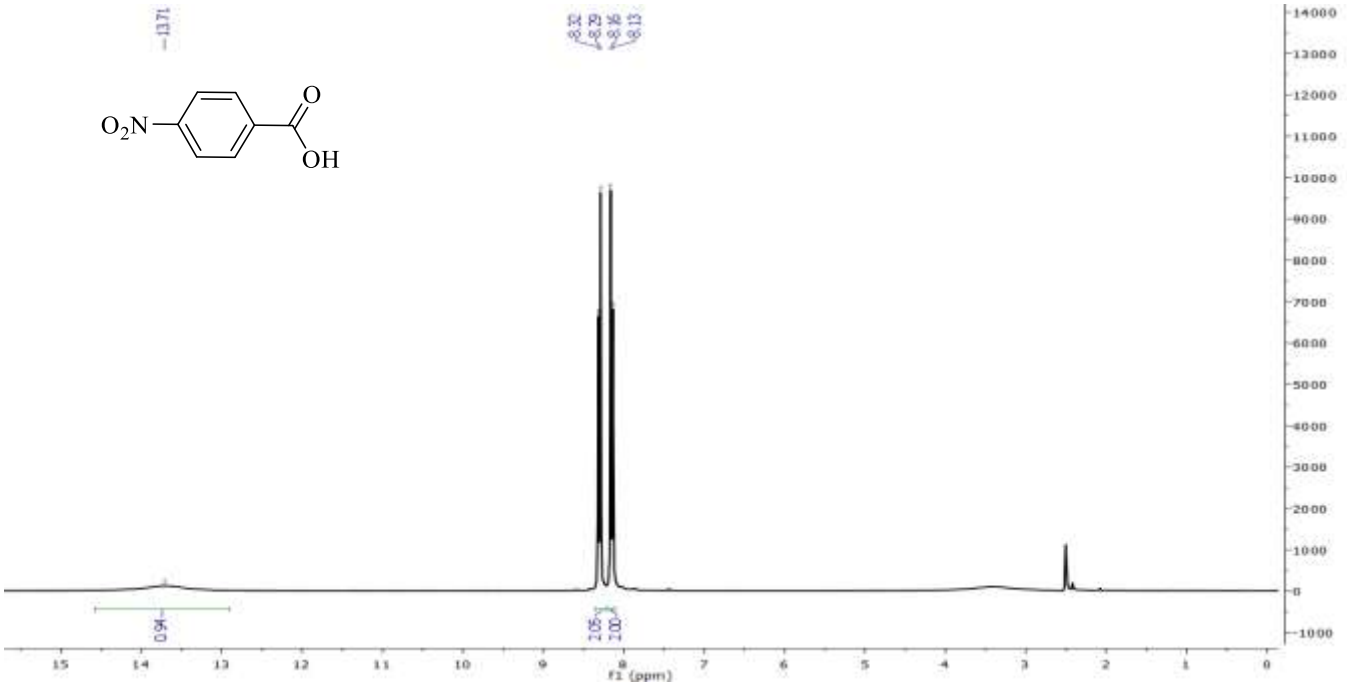

Figure S17. ^{1}H NMR (300 MHz) of *p*-nitrobenzoic acid **6c** in DMSO-*d6*

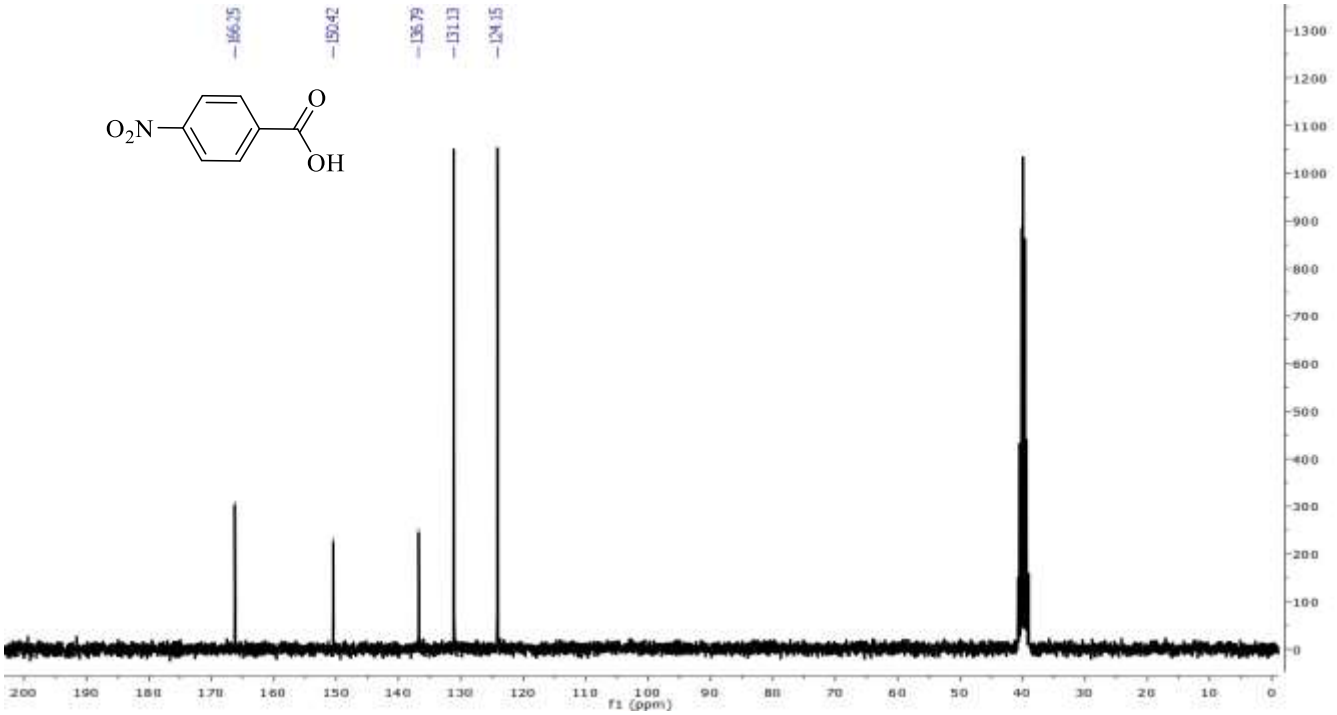

Figure S18. ^{13}C NMR (75 MHz) of *p*-nitrobenzoic acid **6c** in DMSO-*d6*

2.16. ^{1}H and ^{13}C NMR spectroscopies of isatin 3d:

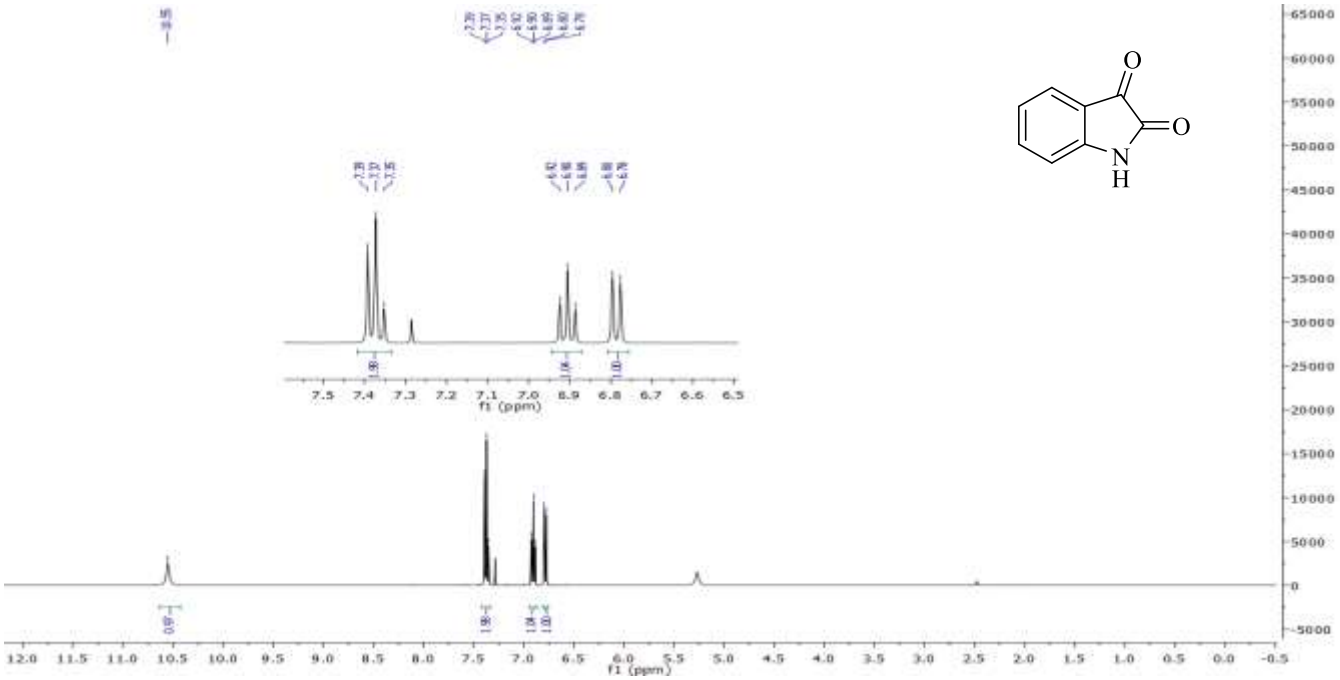

Figure S19. ^{1}H NMR (400 MHz) of isatin **3d** in $CDCl_3$

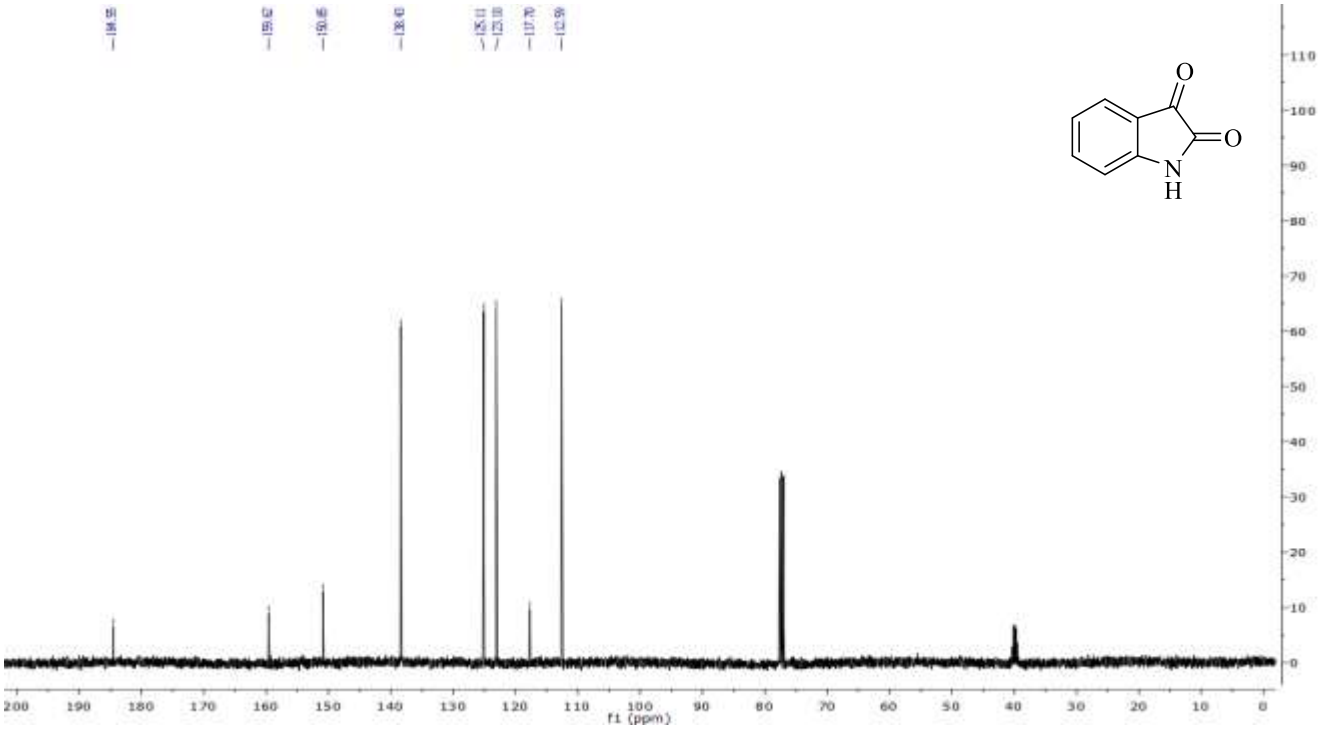

Figure S20. ^{13}C NMR (100 MHz) of isatin **3d** in $CDCl_3$

2.17. Analytical data (HPLC) of the oxidation products:

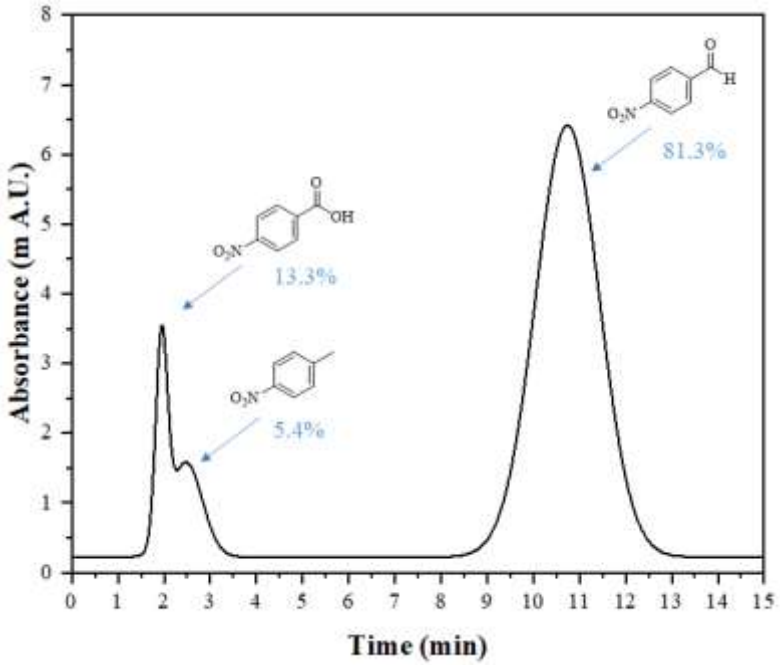

Figure S21. HPLC profile of oxidation *p*-nitro toluene with ([(FcHz)$_2$Ni]) under Blue LED after 48h

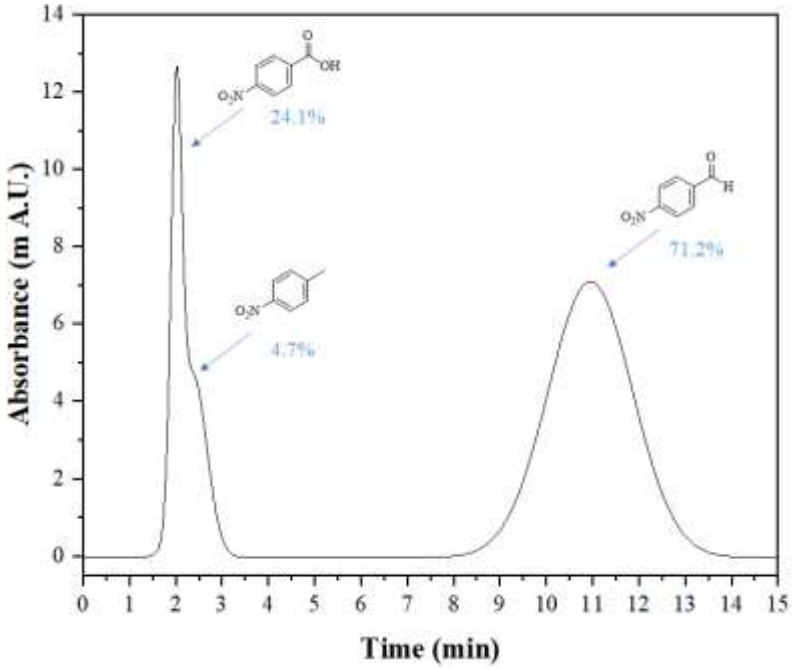

Figure S22. HPLC profile of oxidation *p*-nitro toluene with ([(FcHz)$_2$Ni]) under Violet LED after 48h

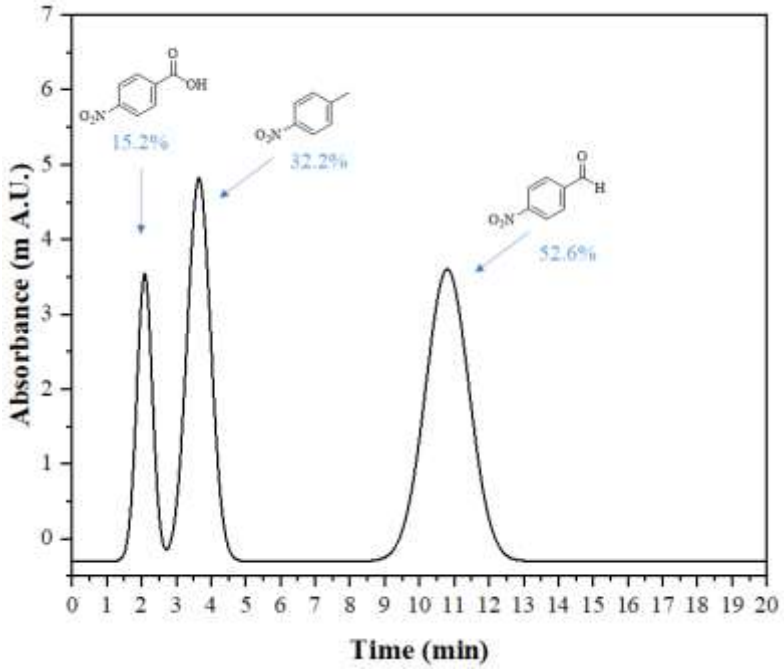

Figure S23. HPLC profile of oxidation *p*-nitro toluene with ([(FcHz)$_2$Ni]) under White LED after 48h

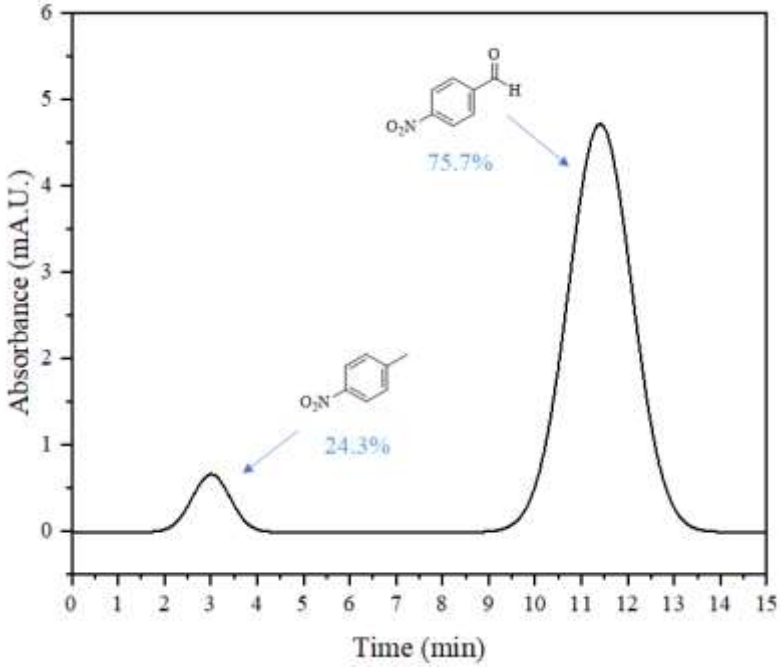

Figure S24. HPLC profile of oxidation *p*-nitro toluene with ([(FcHz)$_2$Ni]) under Green LED after 48h

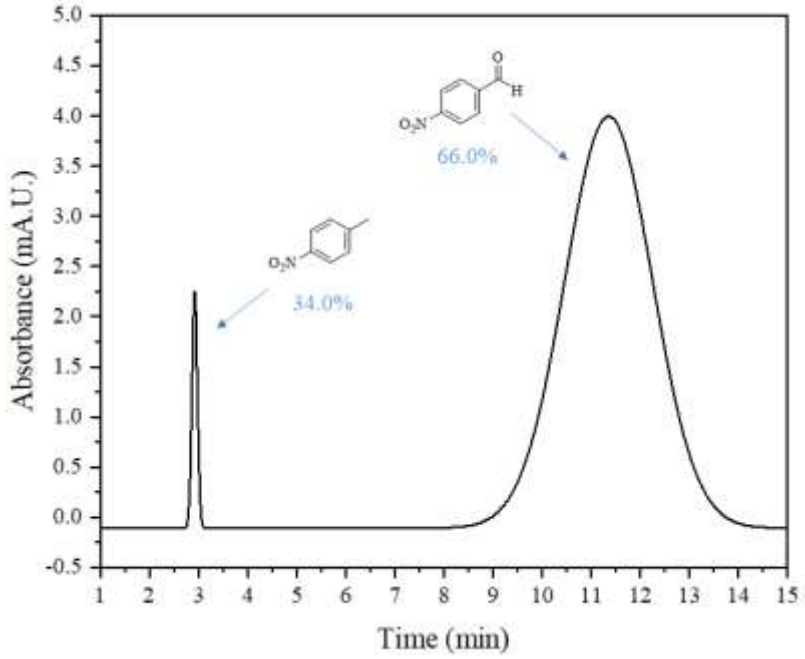

Figure S25. HPLC profile of oxidation *p*-nitro toluene with ([(FcHz)$_2$Ni]) under Red LED after 48h

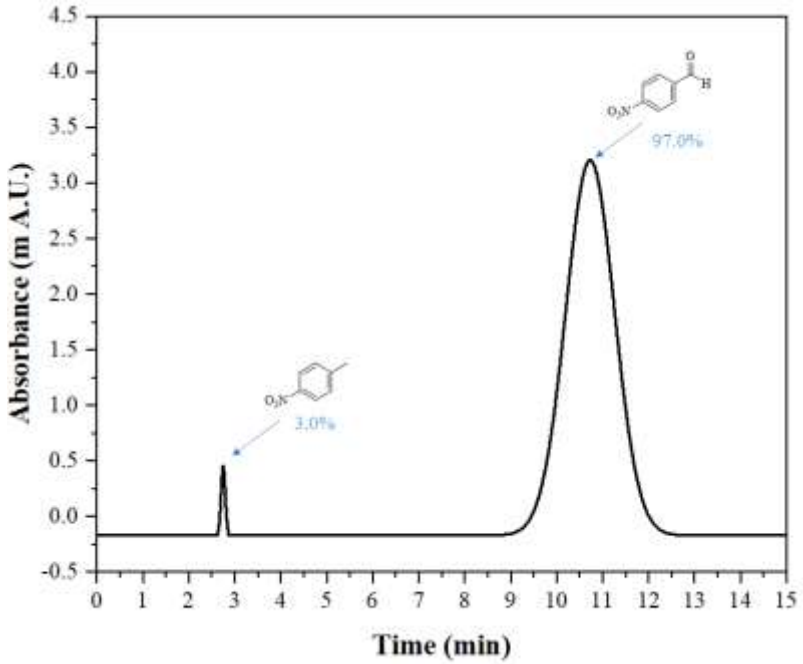

Figure S26. HPLC profile of oxidation *p*-nitro toluene with ([(FcHz)$_2$Cu]) under Blue LED after 48h

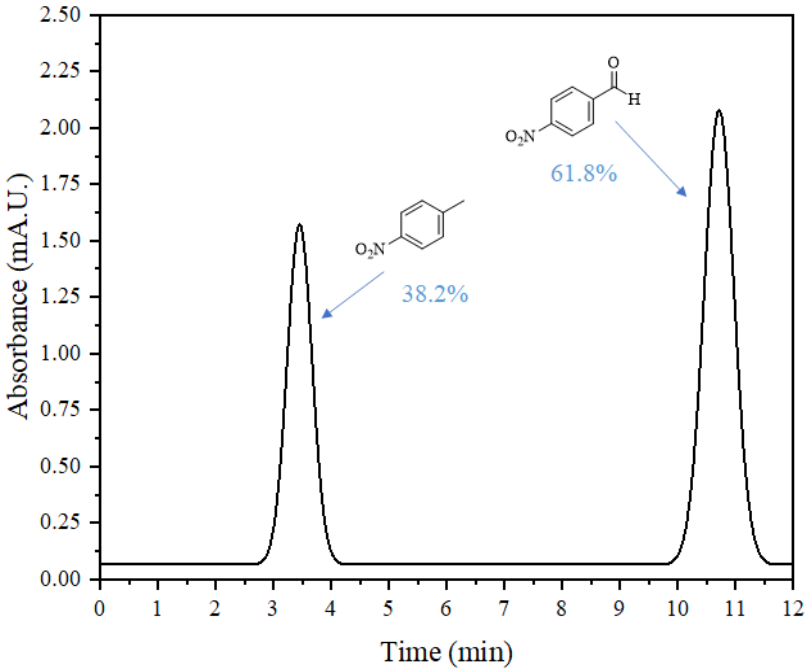

Figure S27. HPLC profile of oxidation *p*-nitro toluene with ([(FcHz)$_2$Cu]) under Violet LED after 48h

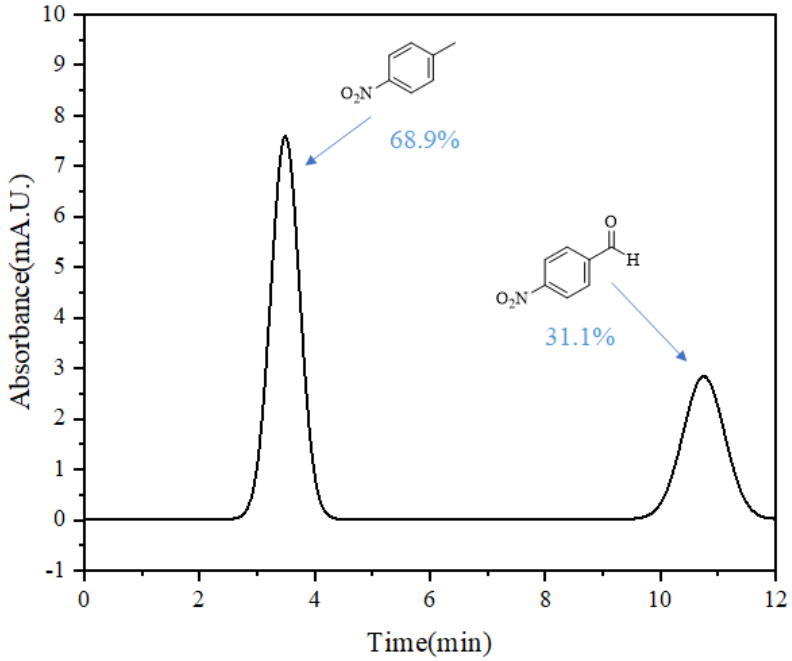

Figure S28. HPLC profile of oxidation *p*-nitro toluene with ([(FcHz)$_2$Cu]) under White LED after 48h

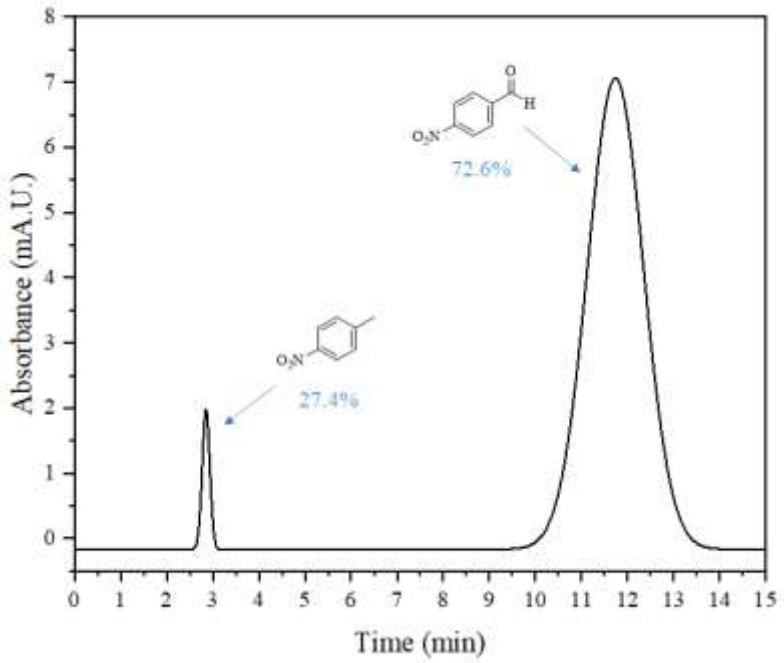

Figure S29. HPLC profile of oxidation *p*-nitro toluene with ([(FcHz)$_2$Cu]) under Green LED after 48h

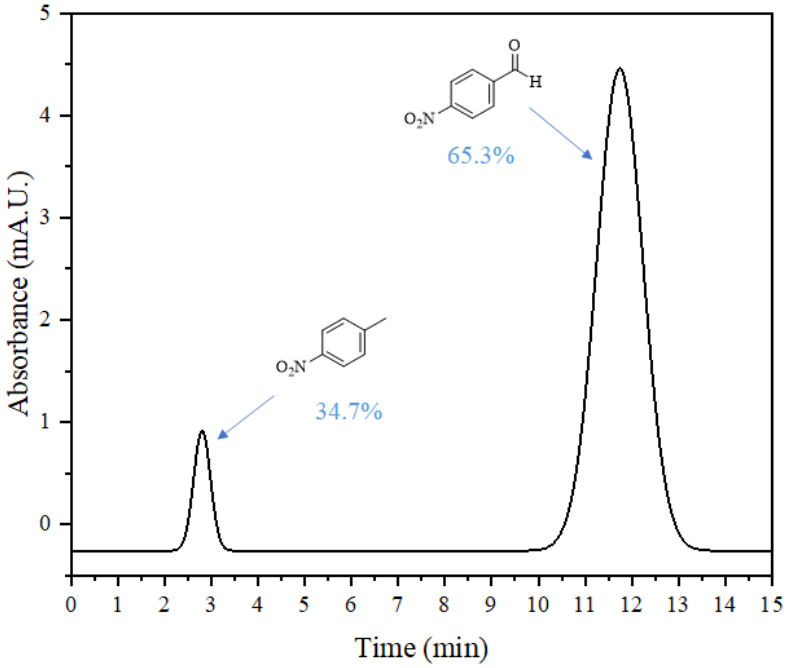

Figure S30. HPLC profile of oxidation *p*-nitro toluene with ([(FcHz)$_2$Cu]) under Red LED after 48h

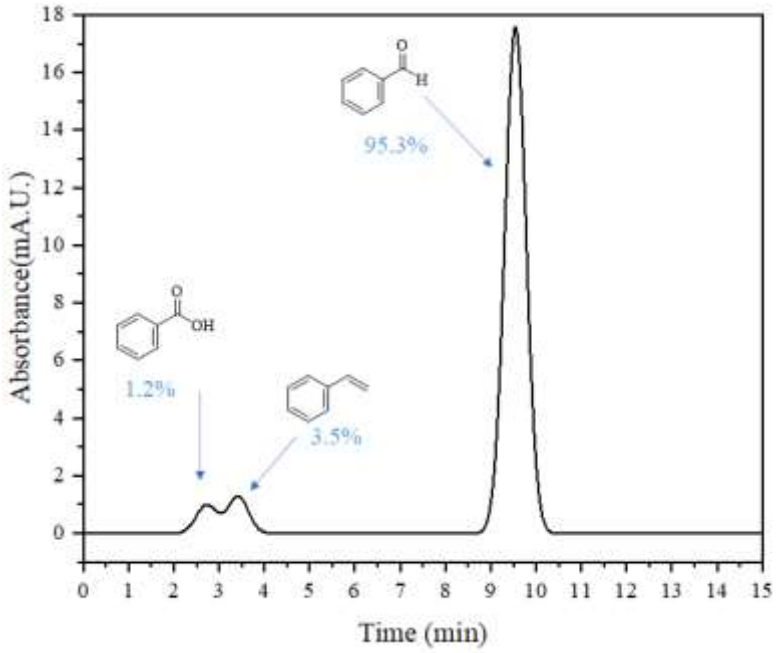

Figure S31. HPLC profile of oxidation styrene with ([(FcHz)$_2$Ni]) under Blue LED after 24h

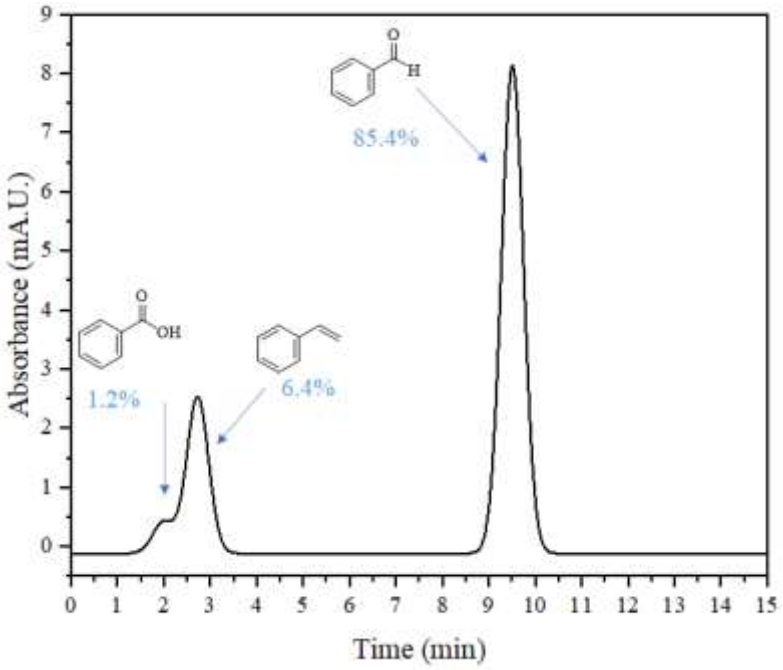

Figure S32. HPLC profile of oxidation styrene with ([(FcHz)$_2$Ni]) under Violet LED after 24h

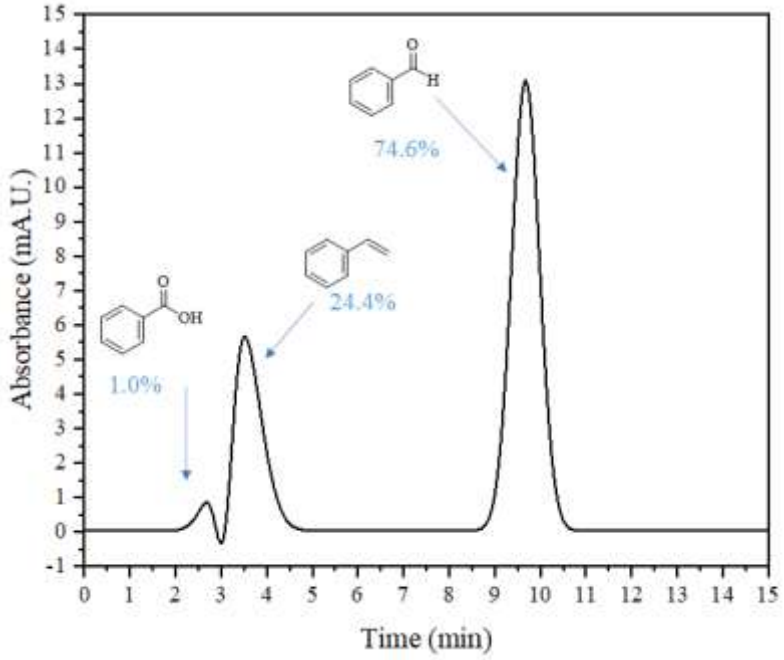

Figure S33. HPLC profile of oxidation styrene with ([(FcHz)$_2$Ni]) under White LED after 24h

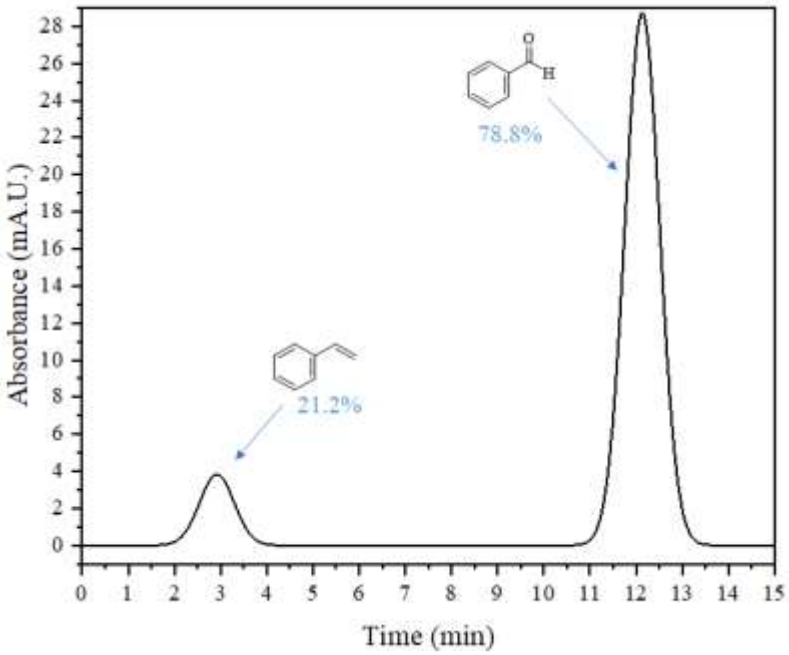

Figure S34. HPLC profile of oxidation styrene with ([(FcHz)$_2$Ni]) under Green LED after 24h

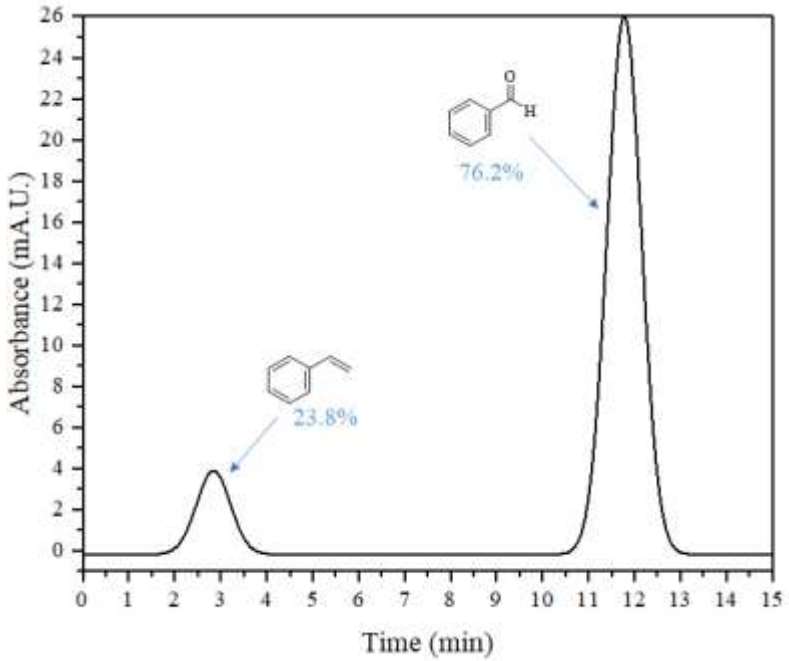

Figure S35. HPLC profile of oxidation styrene with ([(FcHz)$_2$Ni]) under Red LED after 24h

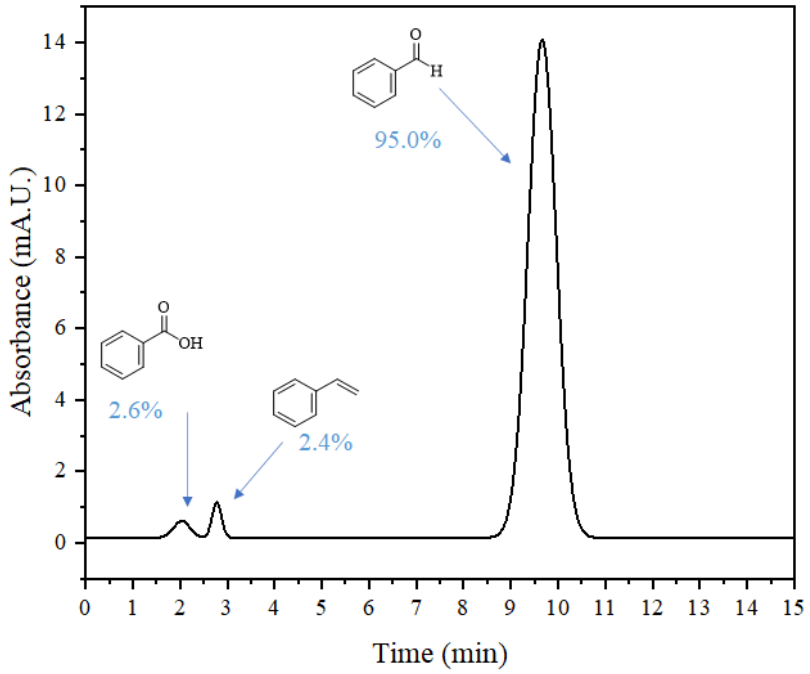

Figure S36. HPLC profile of oxidation styrene with ([(FcHz)$_2$Cu]) under Blue LED after 24h

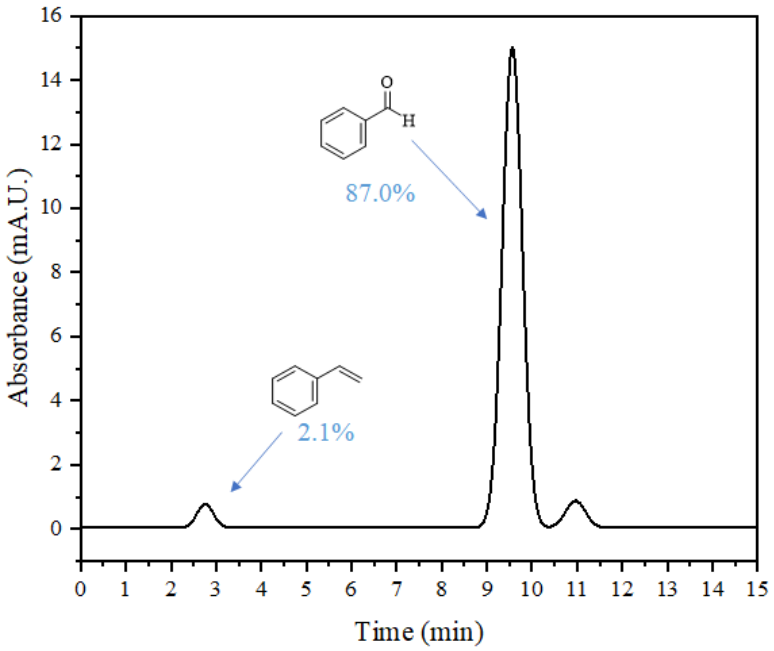

Figure S37. HPLC profile of oxidation styrene with ([(FcHz)$_2$Cu]) under Violet LED after 24h

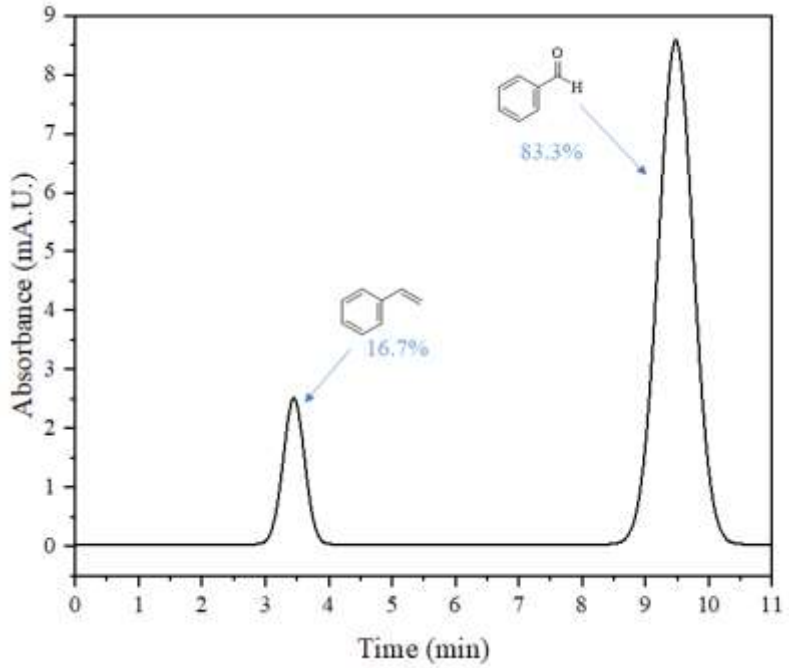

Figure S38. HPLC profile of oxidation styrene with ([(FcHz)$_2$Cu]) under White LED after 24h

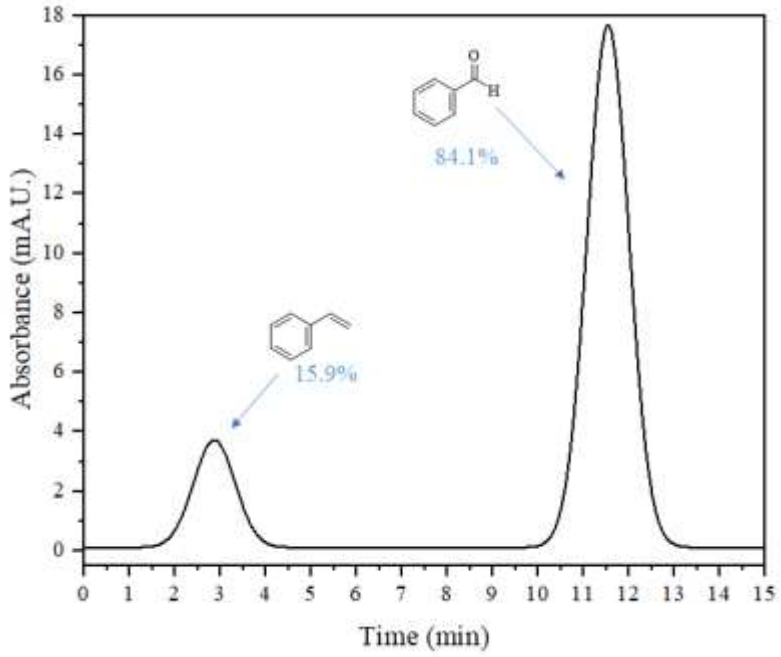

Figure S39. HPLC profile of oxidation styrene with ([(FcHz)$_2$Cu]) under Green LED after 24h

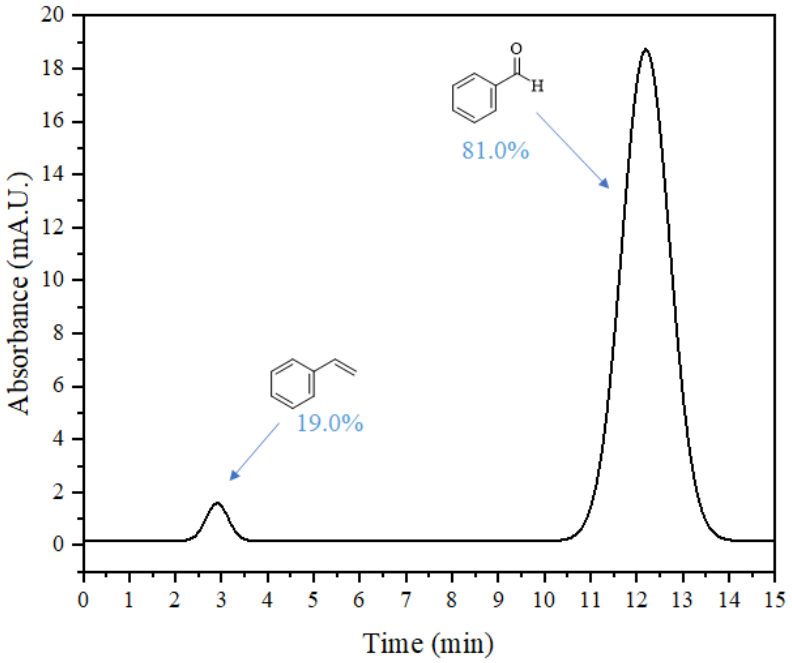

Figure S40. HPLC profile of oxidation styrene with ([(FcHz)$_2$Cu]) under Red LED after 24h

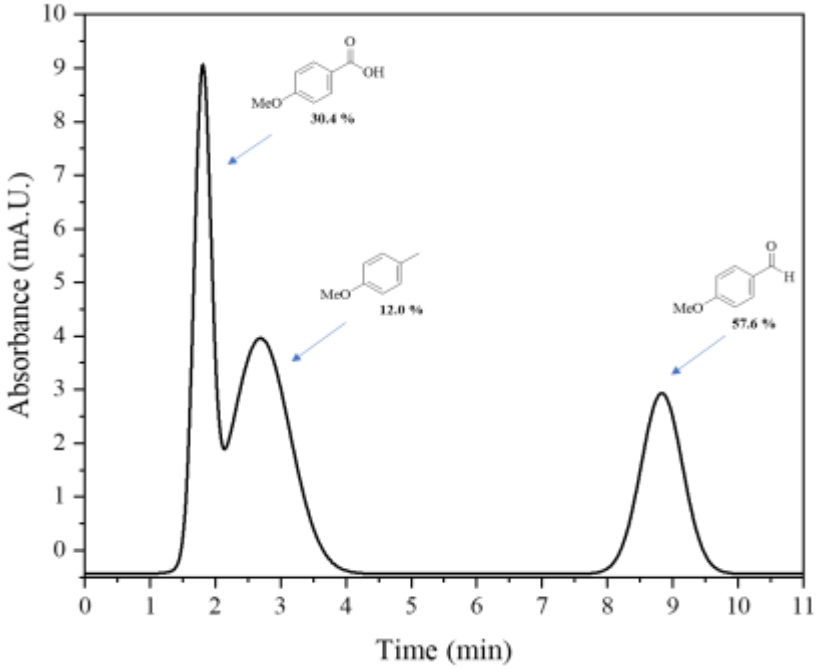

Figure S41. HPLC profile of oxidation *p*-methyl anisole with ([(FcHz)$_2$Ni]) under Blue LED after 48h

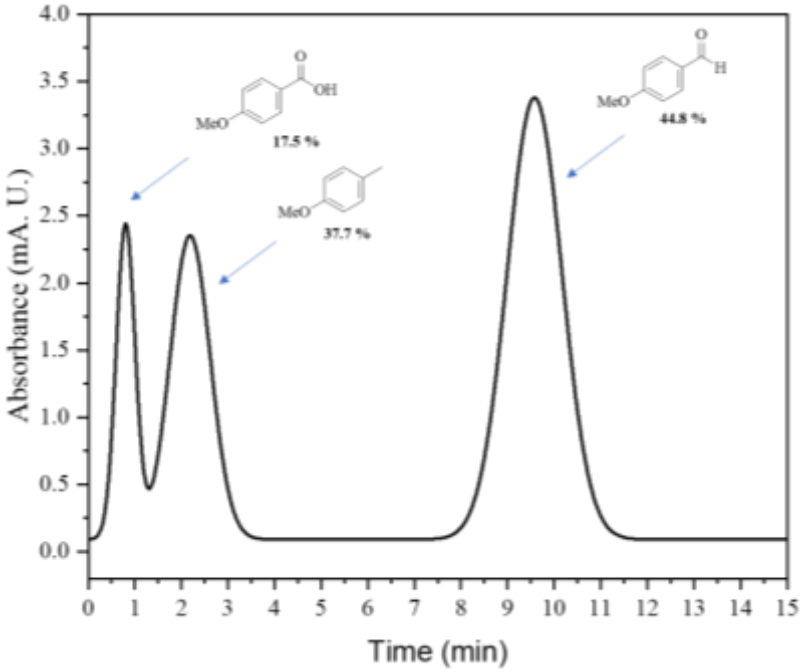

Figure S42. HPLC profile of oxidation *p*-methyl anisole with ([(FcHz)$_2$Ni]) under White LED after 48h

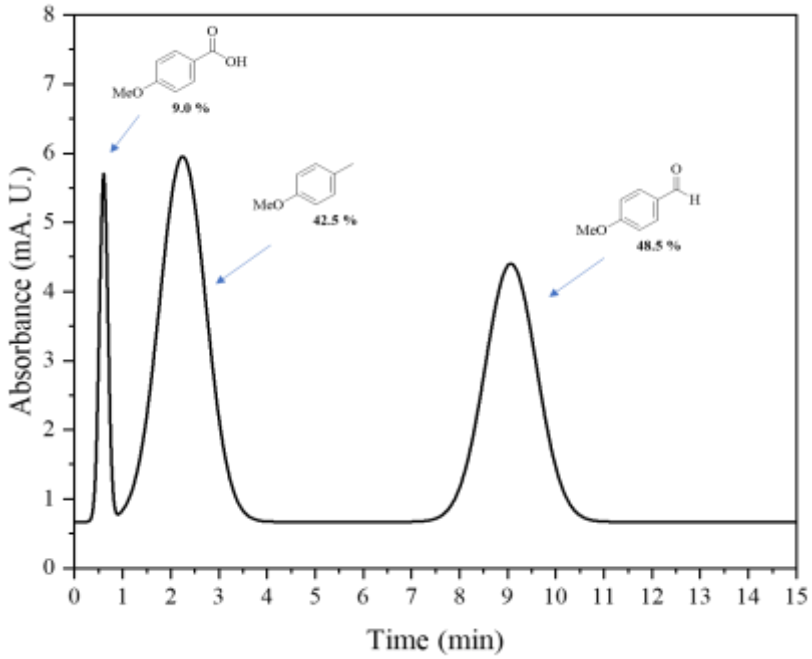

Figure S43. HPLC profile of oxidation *p*-methyl anisole with ([(FcHz)$_2$Ni]) under Green LED after 48h

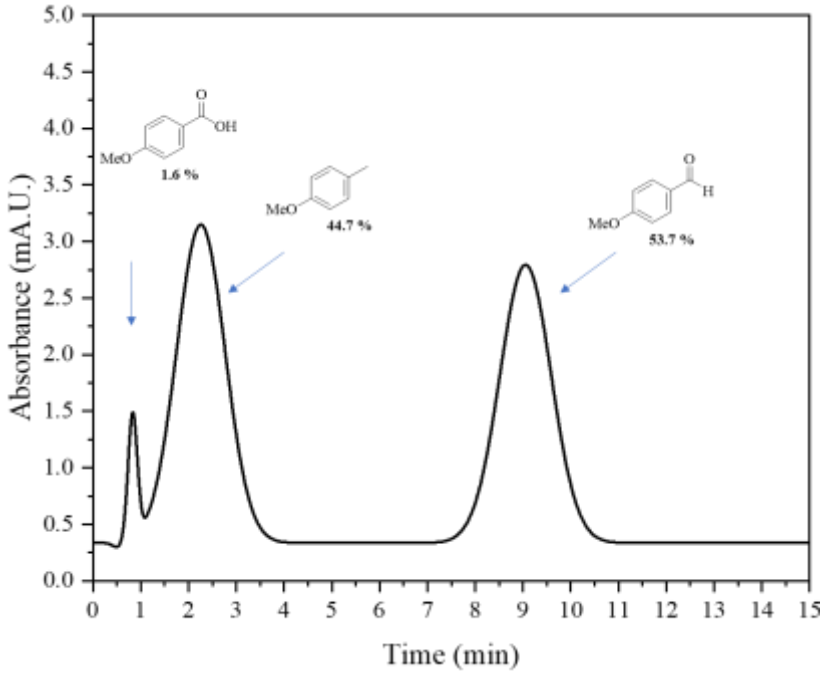

Figure S44. HPLC profile of oxidation *p*-methyl anisole with ([(FcHz)$_2$Ni]) under Red LED after 48h

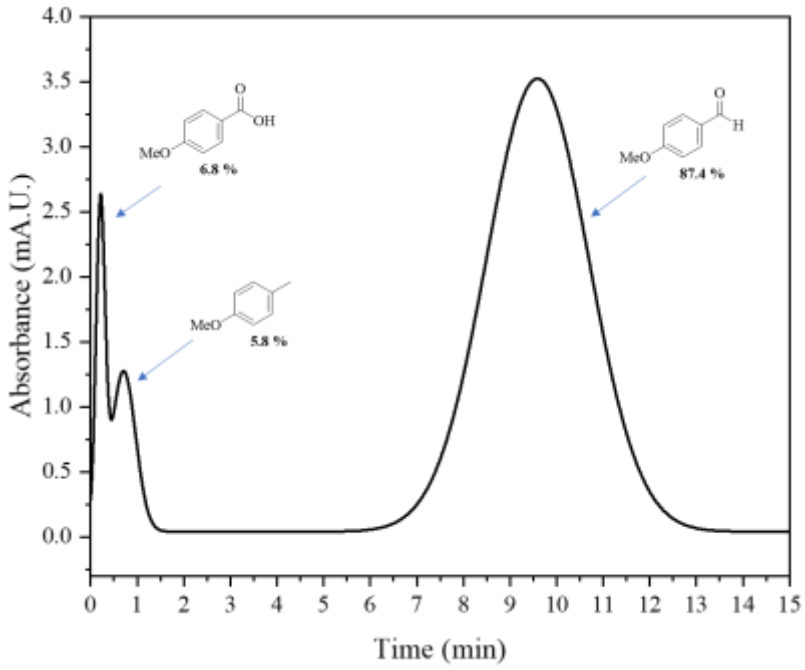

Figure S45. HPLC profile of oxidation *p*-methyl anisole with ([(FcHz)$_2$Cu]) under Blue LED after 48h

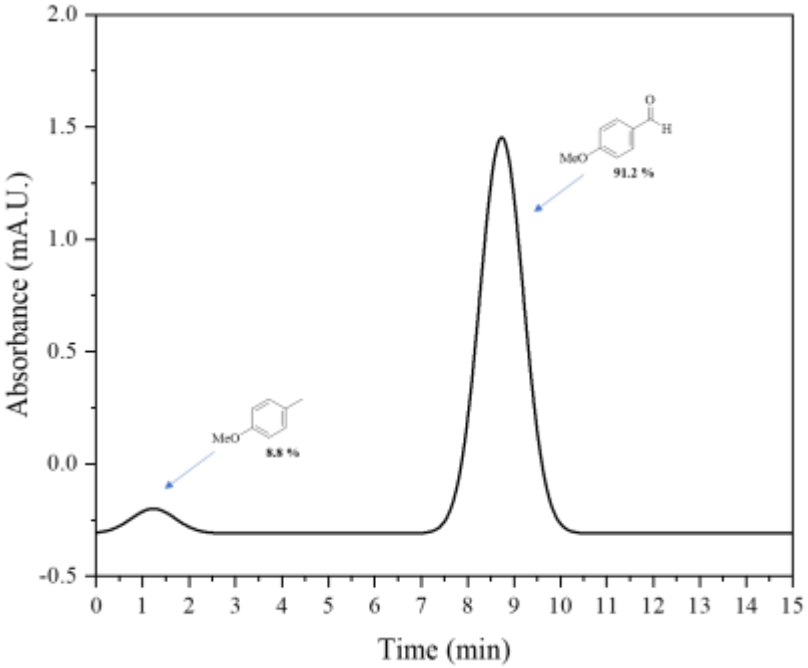

Figure S46. HPLC profile of oxidation *p*-methyl anisole with ([(FcHz)$_2$Cu]) under White LED after 48h

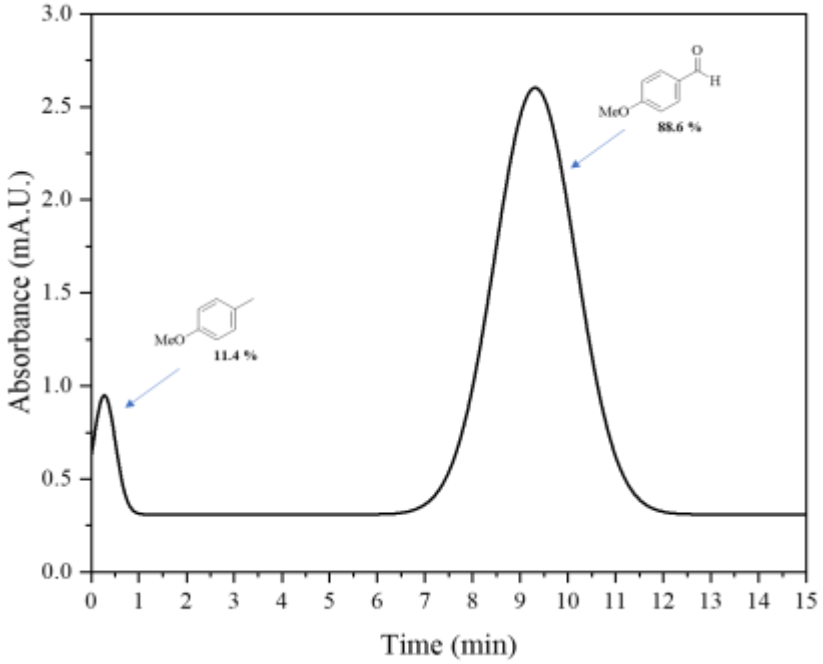

Figure S47. HPLC profile of oxidation *p*-methyl anisole with ([(FcHz)$_2$Cu]) under Green LED after 48h

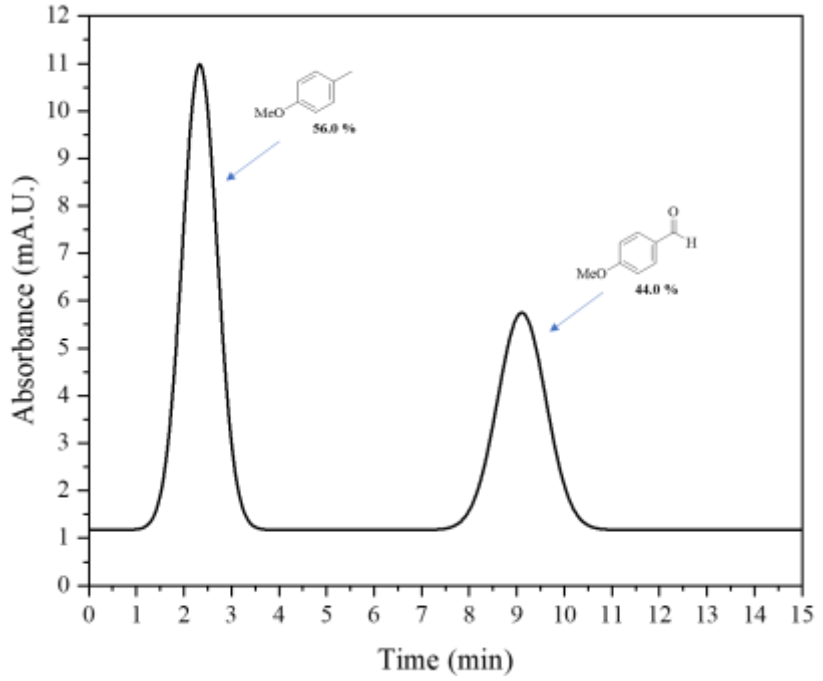

Figure S48. HPLC profile of oxidation *p*-methyl anisole with ([(FcHz)$_2$Cu]) under Red LED after 48h

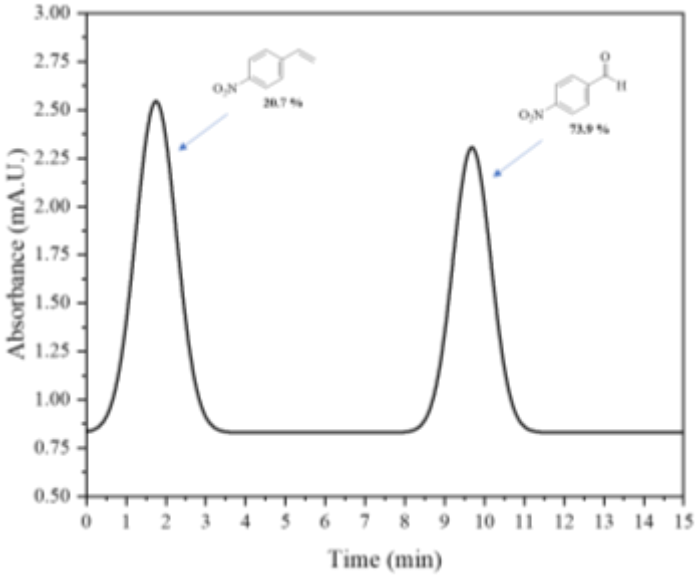

Figure S49. HPLC profile of oxidation *p*-nitro styrene with ([(FcHz)$_2$Ni]) under Blue LED after 24h

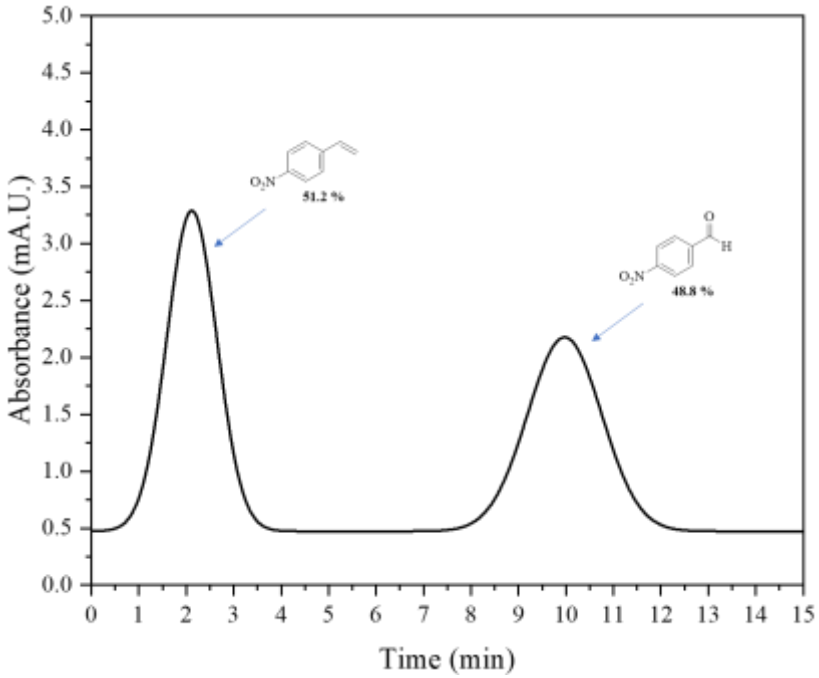

Figure S50. HPLC profile of oxidation *p*-nitro styrene with ([(FcHz)$_2$Ni]) under White LED after 24h

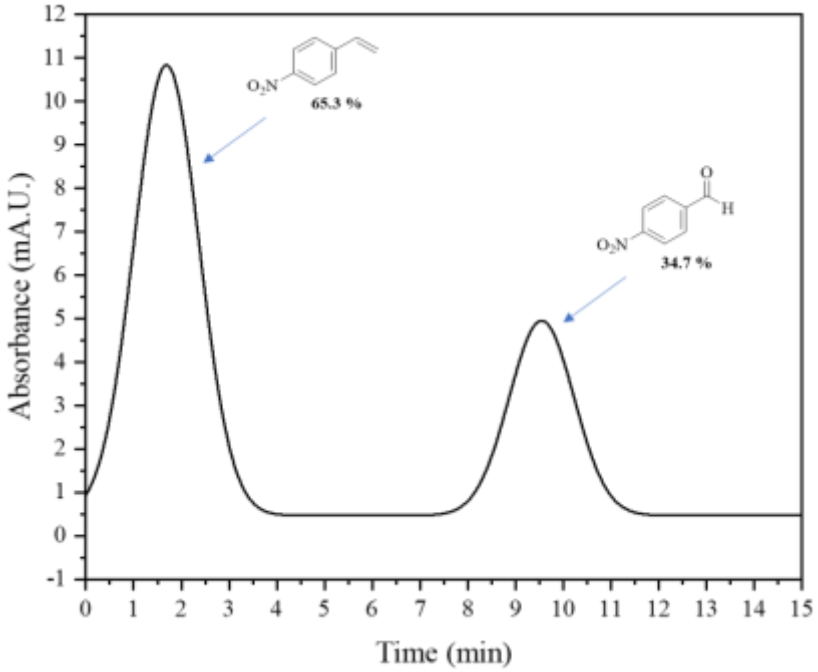

Figure S51. HPLC profile of oxidation *p*-nitro styrene with ([(FcHz)$_2$Ni]) under Green LED after 24h

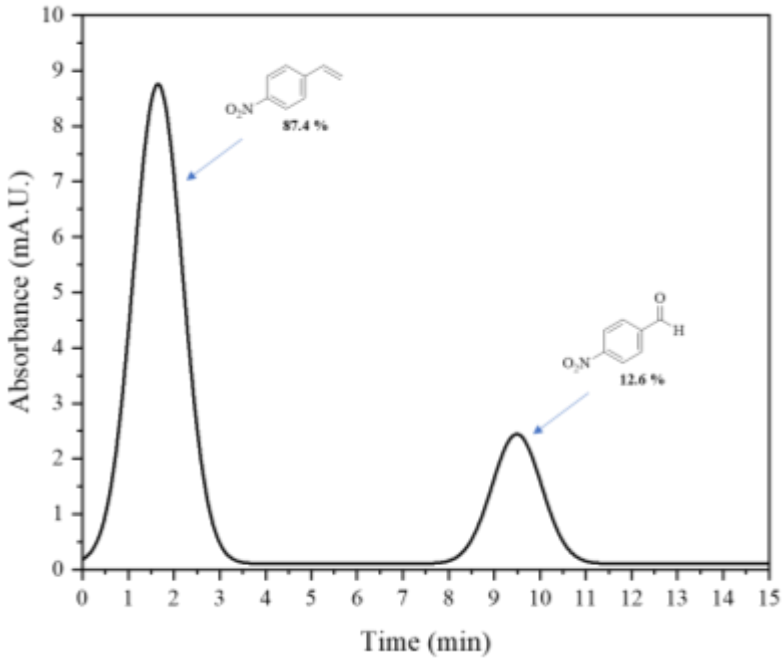

Figure S52. HPLC profile of oxidation *p*-nitro styrene with ([(FcHz)$_2$Ni]) under Red LED after 24h

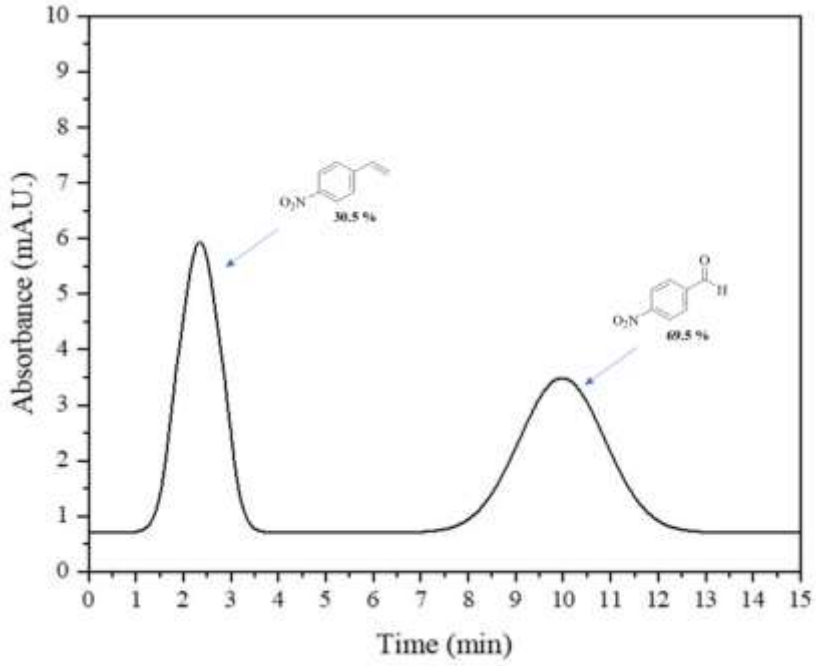

Figure S53. HPLC profile of oxidation *p*-nitro styrene with ([(FcHz)$_2$Cu]) under Blue LED after 24h

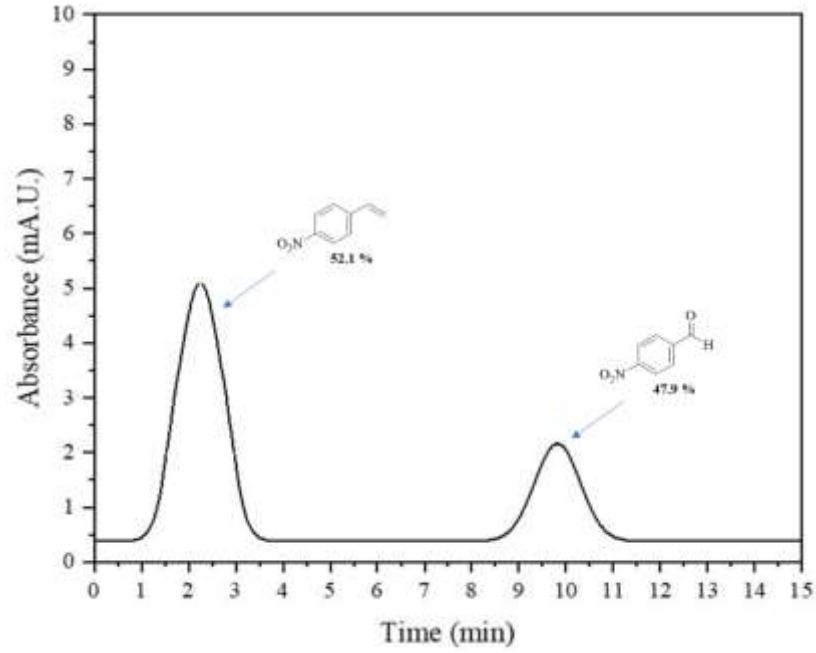

Figure S54. HPLC profile of oxidation *p*-nitro styrene with ([(FcHz)$_2$Cu]) under White LED after 24h

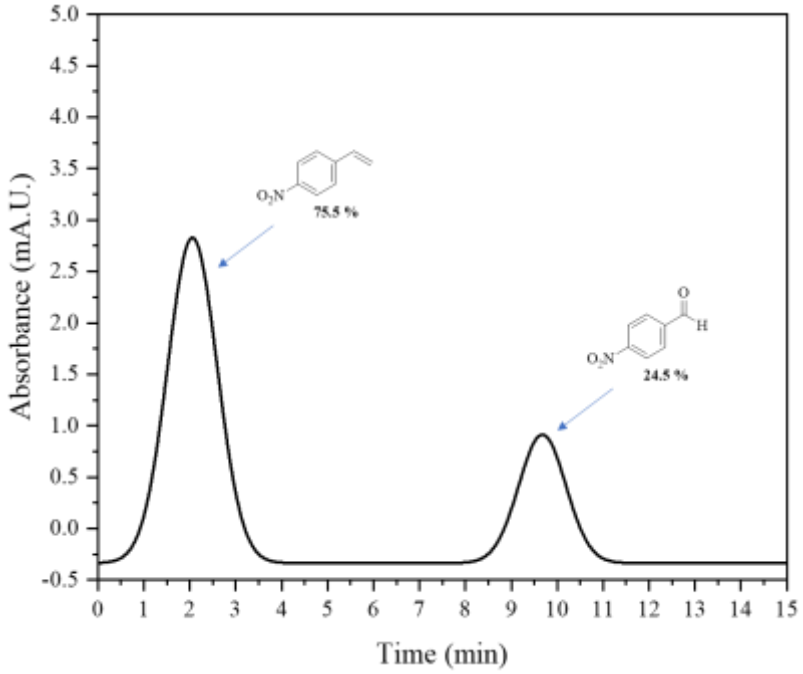

Figure S55. HPLC profile of oxidation *p*-nitro styrene with ([(FcHz)$_2$Cu]) under Green LED after 24h

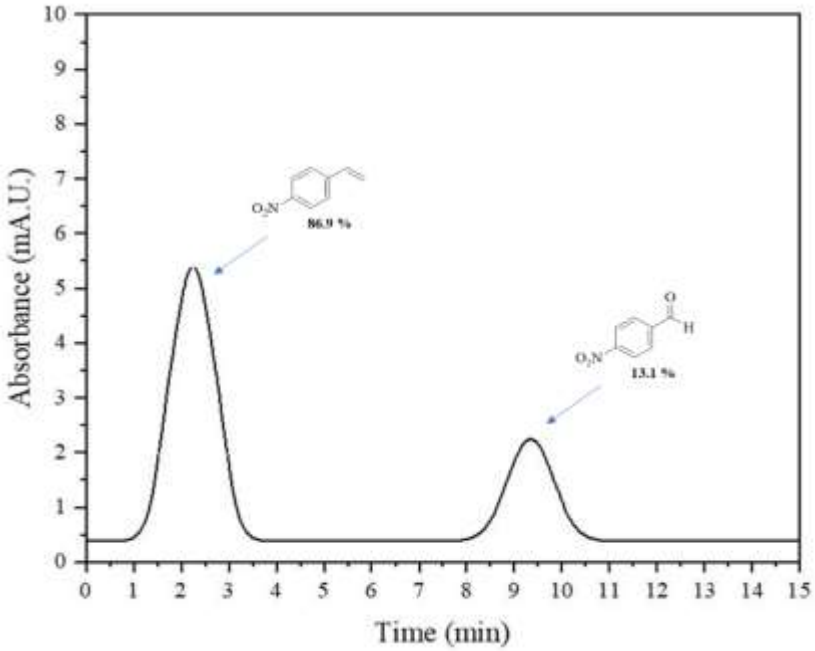

Figure S56. HPLC profile of oxidation *p*-nitro styrene with ([(FcHz)$_2$Cu]) under Red LED after 24h

Investigating the stability of complexes in solution:

A solution containing complexes with a concentration of 10 M was prepared and kept for 24 hours. Subsequently, the UV-visible spectrum of the solution was obtained and compared with the spectrum of their corresponding fresher.

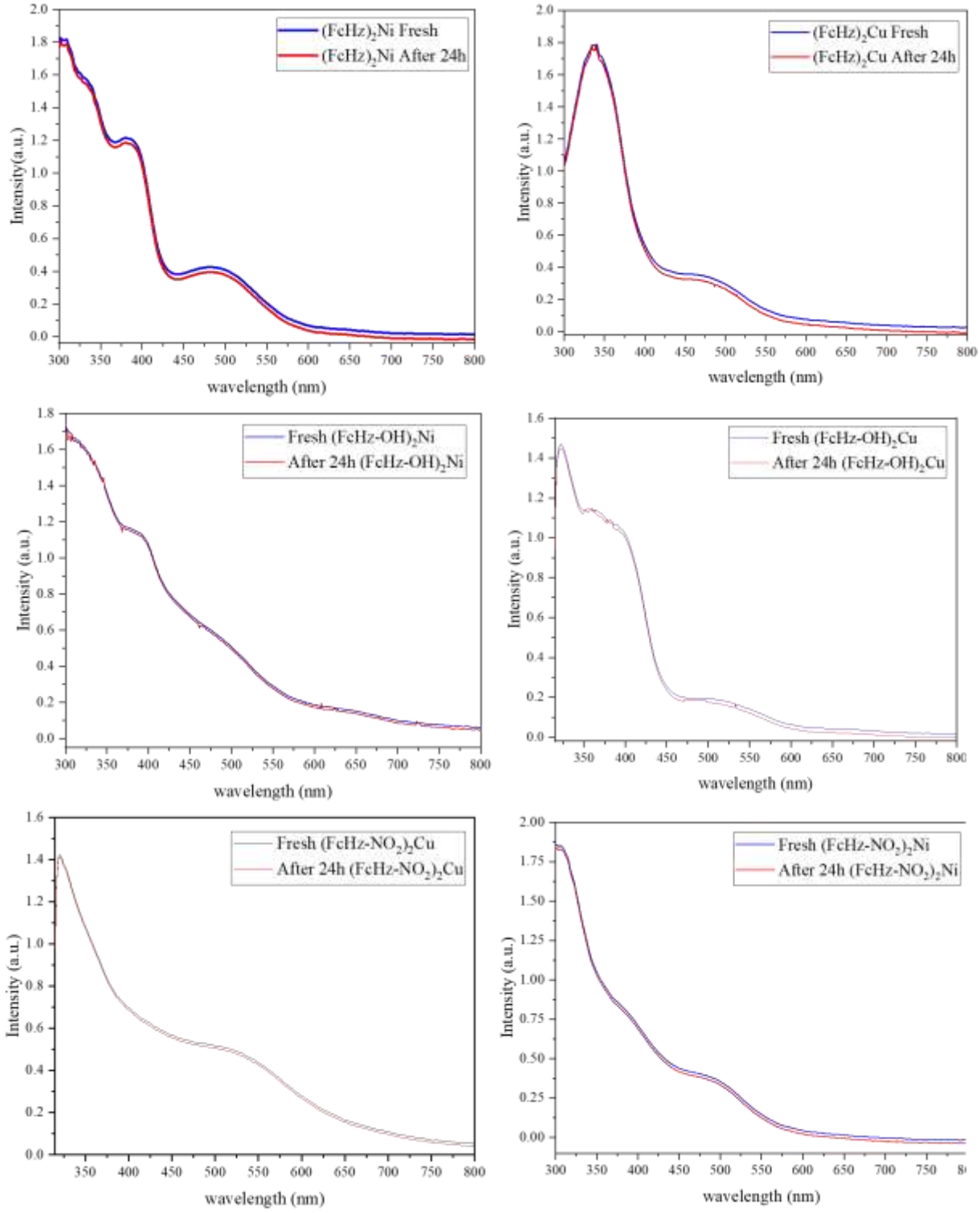

Figure S57. UV-visible spectra of the complexes in fresh and after 24h states

Photoluminescence investigation:

The fluorescence spectral studies provide further evidence of complexation between the ligand and the metal ions in coordination chemistry. The fluorescence excitation spectra of Schiff base 3a-b and their corresponding transition metal complexes were recorded at room temperature, utilizing DMF as the solvent (10^{-6} M). The experimental fluorescence spectra of six kinds of samples were run in DMF as solvent. Emission spectroscopies were recorded in the range of 300-640 nm for FcHz, [$(FcHz)_2Ni$], and [$(FcHz)_2Cu$] as shown in Figure S58. Ferrocene-based complexes FcHz, [$(FcHz)_2Ni$], and [$(FcHz)_2Cu$] were exited at 368, 412, and 485 nm, respectively. The results show that primary imines have a stronger luminescence intensity, and when they are coordinated to metal, their photoluminescence intensity decreases, and in fact, the speed of electron return decreases, which favors photocatalytic reactions. The same observation holds true for the remaining complexes FcHz-OH, [$(FcHz\text{-}OH)_2Ni$], and [$(FcHz\text{-}OH)_2Cu$], with the only noticeable difference being the occurrence of a red shift. This shift can be attributed to the presence of the electron-donating hydroxy group.

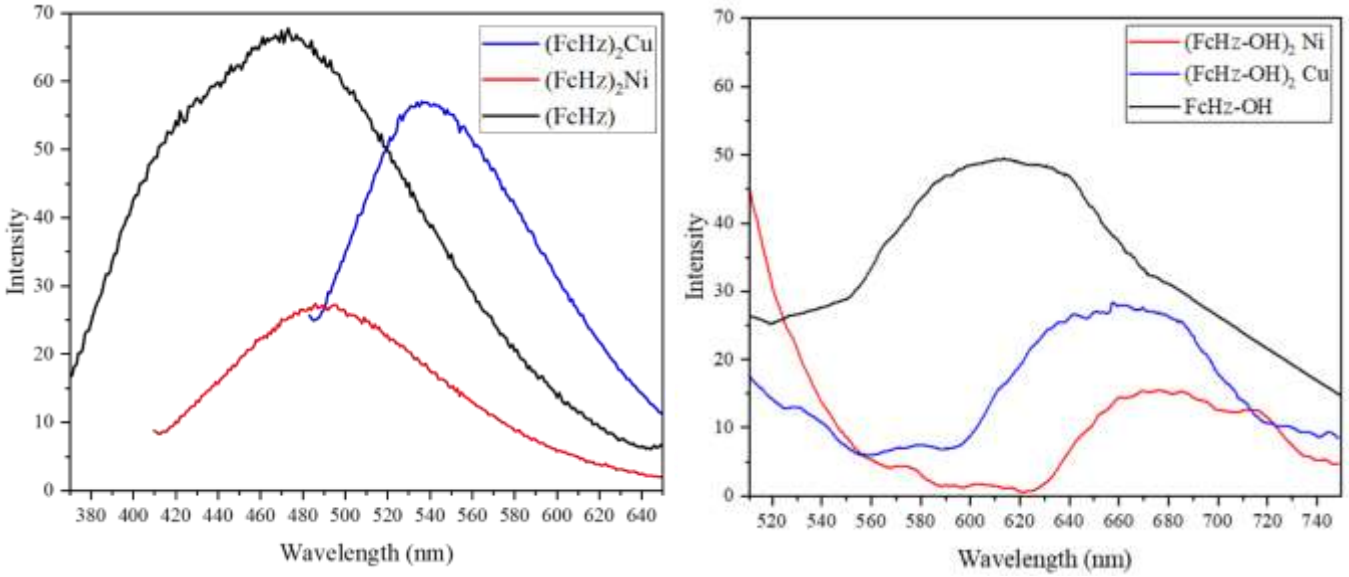

Figure S58. The fluorescence spectra of FcHz, [$(FcHz)_2Ni$], [$(FcHz)_2Cu$] FcHz-OH, [$(FcHz\text{-}OH)_2Ni$], and [$(FcHz\text{-}OH)_2Cu$] complexes

Electrochemical Impedance Spectroscopy (EIS) investigation:

Furthermore, an analysis of electrochemical impedance spectroscopy (EIS) was conducted to extract the impedance properties of synthesized complexes. The results obtained from this analysis are presented in Figure S59. EIS allows for the observation of the charge transfer process and surface reactions of the materials[2]. The diameter of the semicircles in the EIS diagram corresponds to the load transfer resistance of complexes in the respective electrodes[3]. A smaller diameter in the EIS diagram indicates a more efficient charge transfer through the electrode/electrolyte interface[4]. The EIS diagram of metal complexes exhibits a significantly smaller diameter compared to primary imine, suggesting that the coordination of nickel and copper enables the capture of photo-induced electrons[5]. This facilitates more efficient interfacial charge movement between the electrolyte and the electrode, resulting in enhanced conductivity of metal complexes and promoting the effective separation of light-induced electric circuits.

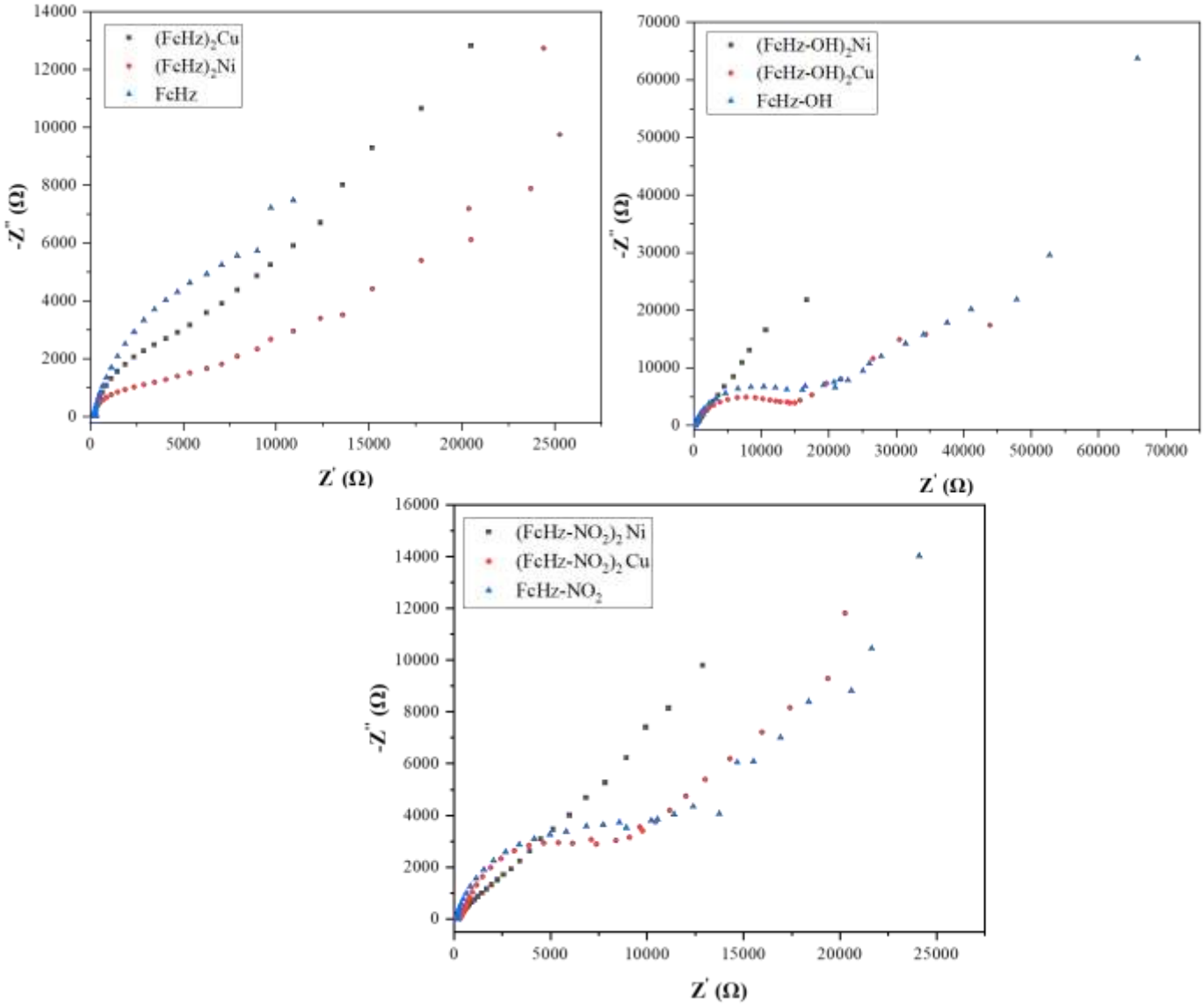

Figure S59. Electrochemical impedance spectroscopy (EIS) results of complexes in probe $K_4Fe(CN)_6$

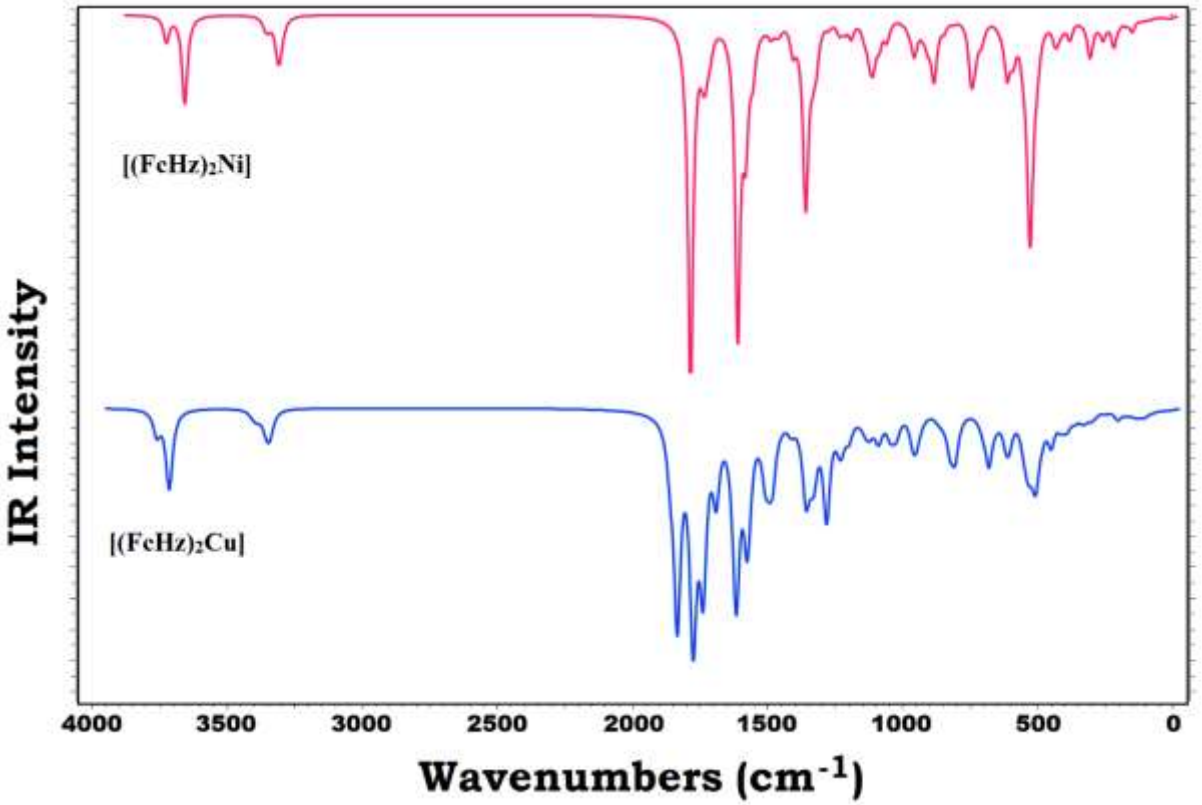

Figure S41. Theoretical IR spectra for $[(FcHz)_2Ni]$ and $[(FcHz)_2Cu]$ complexes computed at ωB97/Def2TZVP level of theory

Table S2. Selected bond distances(Å) and bond angles (deg) for $[(FcHz)_2M]$ and $[(FcHz)_2M]^{2+}$ complexes (M = Ni and Cu) at ωB97/Def2TZVP level of theory in DMF solvent

Bond length	$[(FcHz)_2Ni]$	$[(FcHz)_2Ni]^{2+}$	$[(FcHz)_2Cu]$	$[(FcHz)_2Cu]^{2+}$
$M_{75} - O_{11}$	2.584	1.869	2.339	1.956
$M_{75} - O_{34}$	2.625	1.863	2.341	1.950
$M_{75} - N_8$	1.877	1.889	1.917	1.966
$M_{75} - N_{31}$	1.871	1.885	1.968	1.961
$N_8 - N_{10}$	1.385	1.381	1.382	1.376
$N_{31} - N_{33}$	1.388	1.383	1.378	1.379
$N_8 - C_6$	1.292	1.282	1.366	1.283
$N_{31} - C_{29}$	1.294	1.284	1.283	1.284
$C_3 - C_6$	1.466	1.451	1.431	1.451
$C_{29} - C_{26}$	1.462	1.444	1.456	1.444
$C_{12} - O_{11}$	1.222	1.260	1.249	1.254
$C_{35} - O_{34}$	1.223	1.262	1.225	1.256
$Fe_{75,76} - C_{Fc}$	≈2.03	≈2.03	≈2.03	≈2.03

Bond angle				
$O_{11}-M_{75}-O_{34}$	95.42°	179.58°	112.97°	179.76°
$N_8-M_{75}-N_{31}$	173.67°	179.50°	167.50°	179.39°
$O_{34}-M_{75}-N_{31}$	73.16°	84.01°	73.93°	81.76°
$N_8-M_{75}-O_{11}$	64.54°	83.98°	78.33°	81.69°
$Ni_{75}-N_8-N_{10}$	120.41°	109.57°	113.9°	109.70°
$Ni_{75}-N_{31}-N_{33}$	121.47°	109.64°	118.69°	109.77°
$N_{10}-C_{12}-O_{11}$	123.02°	117.95°	121.75°	119.13°
$N_{33}-C_{35}-O_{34}$	122.60°	117.82°	121.58°	119.03°
Dihedral angle				
$N_{10}-N_8-M_{75}-O_{34}$	95.82°	179.93°	114.87°	179.97°
$N_{10}-N_8-M_{75}-O_{11}$	6.51°	0.25°	4.88°	0.26°
$N_{10}-N_8-N_{31}-N_{33}$	98.85°	179.55°	116.43°	178.69°
$N_{10}-N_8-N_{31}-C_{29}$	61.75°	1.61°	51.72°	1.87°
$O_{11}-C_{12}-C_{13}-C_{14}$	29.49°	20.50°	25.23°	20.56°
$O_{34}-C_{35}-C_{36}-O_{37}$	22.63°	17.64°	21.78°	20.26°
$N_{10}-N_8-C_3-C_4$	25.72°	25.92°	23.73°	25.27°
$N_{10}-N_8-C_{26}-C_{27}$	73.15°	24.29°	89.66°	154.07°
$N_{10}-N_8-N_{31}-C_{29}$	61.75°	1.61°	51.72°	1.87°
$Fe_{76}-C_3-C_{26}-Fe_{77}$	51.94°	120.95°	60.51°	123.89°
$C_{56}-C_3-C_{26}-C_{66}$	56.91°	123.91°	69.68°	127.49°

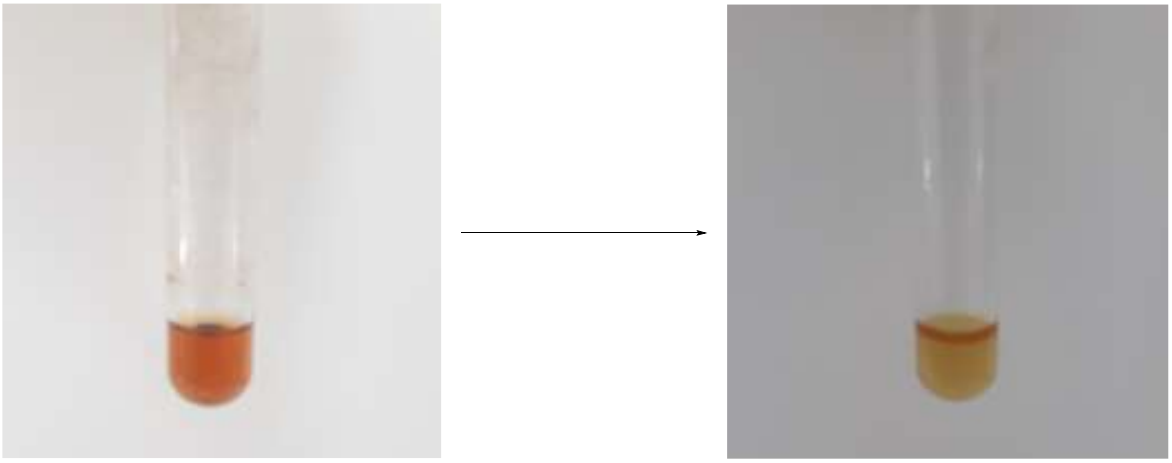

p-nitro toluene products

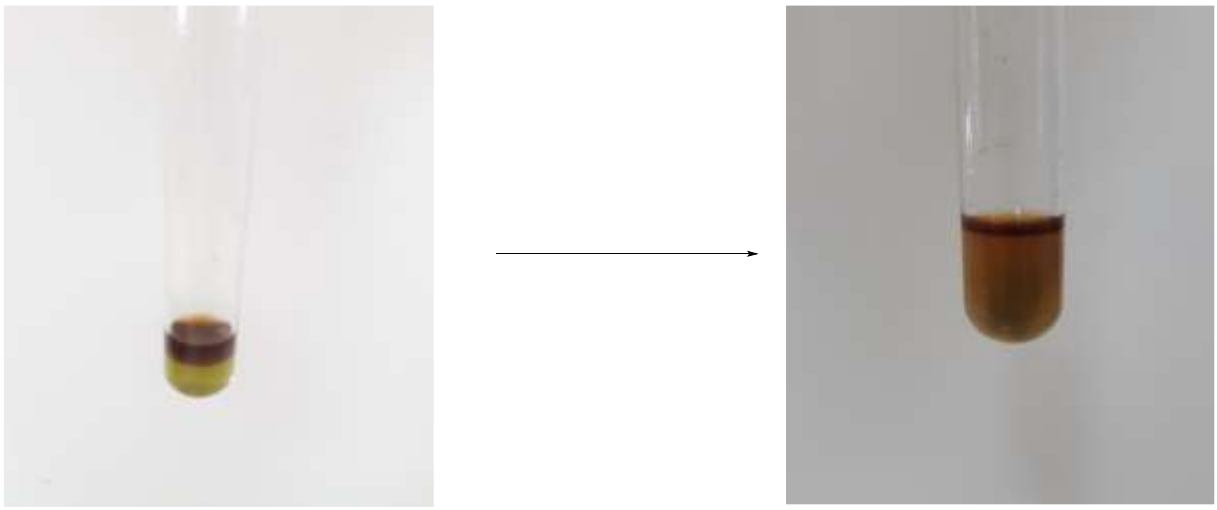

styrene product

References:

1. C. C. Le, M. K. Wismer, Z.-C. Shi, R. Zhang, D. V. Conway, G. Li, P. Vachal, I. W. Davies and D. W. MacMillan, *ACS central science*, 2017, **3**, 647-653.
2. J. Zou, Y. Yu, K. Qiao, S. Wu, W. Yan, S. Cheng, N. Jiang and J. Wang, *Journal of Materials Science*, 2020, **55**, 13618-13633.
3. T. Alizadeh, S. Nayeri and N. Hamidi, *RSC advances*, 2019, **9**, 13096-13103.
4. T. Ma, Q. Shen, B. Zhaoa, J. Xue, R. Guan, X. Liu, H. Jia and B. Xu, *Inorganic Chemistry Communications*, 2019, **107**, 107451.
5. E. Sedlackova, Z. Bytesnikova, E. Birgusova, P. Svec, A. M. Ashrafi, P. Estrela and L. Richtera, *Materials*, 2020, **13**, 4936.